

Weighted efficiency optimization of flyback micro-inverter under improved boundary conduction mode (i-BCM)

Anastasios Ch. Nanakos, Georgios C. Christidis, *Student Member, IEEE*, and Emmanuel C. Tatakis

Abstract— The flyback topology is proven to be a very strong candidate solution for use in ac-PV module applications. Operation in the Boundary Condition Mode (BCM) provides high power density while maintaining the characteristics of a current source inverter. In this paper, a design methodology is presented, that maximizes the weighted efficiency of the converter through an optimization algorithm. The inverter operation is investigated and the behavior under the improved BCM is documented by analytical equations followed by the power loss calculations for each component. This enables to accurately define the relation between the design parameters and the efficiency of the implemented converter and so, an optimization algorithm is established, that takes into consideration the design specifications and constraints. The proposed methodology is also verified with an experimental prototype.

Index Terms—AC-PV module, DC-AC power conversion, Design methodology, Energy efficiency, Losses, Magnetic losses, Micro-inverter, Photovoltaic power systems

NOMENCLATURE

V_{dc}	Input voltage (V).
V_{acp}	Peak voltage value of the utility grid (V).
$V_{ac,i}$	Mean voltage value of the utility grid during each switching cycle i (V).
$P_{PV,nom}$	Nominal inverter input power (W).
$w(\%)$	Predefined power ratio according to European and CEC efficiency evaluation procedures.
$P_{PV,w}$	Input power defined by ratio w (W).
η_{EUR}	The weighted European MPPT efficiency.
η_{CEC}	The weighted CEC MPPT efficiency.
$r_{loss,w}$	Power loss ratio.
η_w	Efficiency at the power level defined by w .
$P_{loss,w}$	Absolute value of power losses at the power level defined by w (W).
$T_{s,i}$	Switching period of the primary switch during each switching cycle (s).
$T_{s,p}$	Peak switching period of the primary switch (s).

T_{hl}	Rectified line period (s)
t_m	Sum of all the switching periods that occur during one rectified line period (s)
m	Number of switching periods within T_{hl}
$t_{on,i}$	Primary switch ON-time during each switching cycle i (s).
$t_{off,i}$	Primary switch OFF-time during each switching cycle i (s).
$t_{on,p}$	$t_{on,i}$ interval value referring to the switching cycle that occurs at the time-area of $\omega t = 90$ (s).
$f_{s,max}$	Maximum switching frequency of primary switch (Hz).
$f_{s,min}$	Minimum switching frequency of primary switch (Hz).
$f_{s,avg}$	Average switching frequency of primary switch (Hz).
i_{pri}	Instant current value of the primary transformer side (A).
i_{sec}	Instant current value of the secondary transformer side (A).
$I_{pri,avg}$	Average current value of the primary transformer side (A).
$I_{sec,avg}$	Average current value of the secondary transformer side (A).
$I_{pri,rms}$	RMS current value of the primary transformer side (A).
$I_{sec,rms}$	RMS current value of the secondary transformer side (A).
$I_{pri,p,i}$	Peak current value of the primary transformer side during each switching cycle i (A).
$I_{sec,avg,i}$	Average current value of the secondary transformer side during each switching cycle i (A).
$I_{sec,avg,p}$	Average current value of the secondary transformer side referring to the switching cycle that occurs at the time-area of $\omega t = 90$ (A).
$I_{sec,p,i}$	Peak current value of the secondary transformer side during each switching cycle i (A).
$V_{sp,i}$	Peak voltage value on the main MOSFET during each switching cycle i (V).
$I_{sp,i}$	Peak current value of the main MOSFET during each switching cycle i (A).
$V_{ir,sec,max}$	Maximum voltage on the transistors on the secondary transformer side (V).
$V_{ir,BD}$	Breakdown voltage of the secondary transformer side switches (V).

Manuscript received May 3, 2014; revised June 29, 2014 and September 22, 2014; accepted November 3, 2014. Date of current version November 10, 2014.

The authors are with the Department of Electrical and Computer Engineering, Laboratory of Electromechanical Energy Conversion, University of Patras, Rion-Patras 26504, Greece (e-mail: tnanakos@ece.upatras.gr; gchristidis@ece.upatras.gr; e.c.tatakis@ece.upatras.gr)

L_I	Transformer primary inductance (μH).
l_g	Length of the core air gap (cm)
$R_{ds,pri}$	ON-resistance of the transistor on the primary transformer side (Ω).
$R_{ds,sec}$	ON-resistance of the transistor on the secondary transformer side (Ω).
$t_{f,pri}$	Current fall time of the switch on the primary transformer side (ns).
V_d	Diode forward voltage (V).
$A_{w,Cu}$	Area of the winding window filled by copper (mm^2).
V_e	Effective core volume (mm^3).
A_e	Effective cross sectional area of the core (mm^2).
R_t	Thermal resistance of the transformer core from the external ambient to the central hot spot ($^{\circ}\text{C}/\text{W}$).
α, β, k	Parameters of the Steinmetz equation loss formula.
B_p	Maximum operational flux density (mT).
B_{sat}	Saturation limit of the flux density (mT).
r	Radius of the winding copper strand (mm).
str_{pri}	Number of strands of the primary winding.
str_{sec}	Number of strands of the secondary winding.
J	Current density of the transformer windings (A/mm^2).
N_{pri}	Number of turns of the transformer primary winding (PV-side).
n	Transformer turns ratio value.
Fr_z	Resistance factor of the winding z.
$R_{ac,z}$	Effective resistance of winding z (Ω).
$R_{dc,z}$	Resistance of winding z at direct current of constant value (Ω).
$I_{z,rms}$	Rms current of the winding z (A).
$I_{z,avg}$	Average current of the winding z (A).
E_i	Energy switching losses of the semiconductor on the primary transformer side during each switching cycle i (J).
$P_{SL,SW,pri}$	Switching losses of the semiconductor on the primary transformer side (W).
$P_{CL,SW,pri}$	Conduction losses of the semiconductor on the primary transformer side (W).
$P_{CL,SW,sec}$	Conduction losses of the semiconductor on the secondary transformer side (W).
$P_{CL,d}$	Conduction losses of the diode (W).
$P_{CRL,i}$	Transformer core losses during each duty cycle i (W).
P_{CRL}	Transformer core losses (W).
P_{CuL}	Transformer copper (windings) losses (W).
DT	Transformer temperature rise ($^{\circ}\text{C}$).
DT_{max}	Maximum allowed transformer temperature rise ($^{\circ}\text{C}$).
C_{ff}	Percentage of the copper area over the entire winding window.
C_{ffmax}	Maximum allowed percentage of the copper area over the entire winding window.
L_f	Output filter inductance (H).
C_f	Output filter capacitance (F).

I. INTRODUCTION

THE photovoltaic (PV) systems have gained, in the last two decades, an increasing interest, due to the price rise of fossil fuels, the increased power demand, as well as the adoption of clean and renewable energy sources. There are three separate markets for the penetration of this technology: large scale high power photovoltaic plants (ranging up to several megawatts) in regions where there is high solar insolation, medium scale PV systems (ranging from tenths to hundredths of kilowatts), mainly for professional use and finally, small scale, decentralized grid connected PV systems, like the ac-PV modules [1]. This most recent technology is oriented to the user who wants to effortlessly and safely install a few solar panels to any building's rooftop. For this reason, every panel has an integrated single phase power electronics inverter, which implements MPPT control and anti-islanding protection. Thus, maximum power generation is achieved, even with partial shadows, and the system is easily upgradable at any time.

Many converter topologies have been proposed for the ac-PV modules [2]-[5]. Among those, the flyback inverter has been the center of attention, since, not only does it satisfy the application requirements (high voltage step-up, transformer isolation, low volume, high reliability), but it also provides high efficiency and relatively simple control. Research teams have focused on different areas of the flyback converter, such as the accuracy of the MPPT algorithm [6]-[7], anti-islanding techniques [8]-[10], methods for power decoupling in order to minimize the value of the input capacitor [11]-[15] or ways to improve the converter THD and power factor [16]-[18].

Another point of interest for the flyback inverter is the mode of operation. The widely used Discontinuous Conduction Mode (DCM) [19]-[20] is the simplest controlled mode, requiring the fewest number of sensors. However, since the transformer must be completely demagnetized on each switching cycle, the power density of the converter is limited. The Continuous Conduction Mode (CCM) has been recently proposed for use on the flyback inverter [21]-[23], but it demands more sensors and the control algorithm is significantly more complex. Finally, the third mode of operation is the Boundary Conduction Mode (BCM), in which, the transformer is momentarily demagnetized on each switching cycle [19]. An improved switching modulation technique for the converter under BCM was recently proposed [24]-[25]. The improvement focuses on minimizing the output current THD and injecting pure sinusoidal current to the grid.

In order to limit the power losses of the flyback inverter, many different methods have been proposed [26]-[28] so as to exploit the energy of the transformer leakage inductance that would normally be dissipated, or ensure soft-switching for the semiconductor devices. A different proposed course of action is the adoption of the interleaved design [29]-[33] which, however, increases the cost of the converter and decreases its reliability.

On the contrary, very few research papers have focused on the selection of the design parameters in order to achieve a global optimization of the converter as it is described by the

weighted efficiency [34]. Therefore, the converter can be built to have an optimal performance for the whole operating range of the PV panel, as its provided power varies during the day. In [35] a methodology to determine the design parameter values, in order to minimize power losses and optimize the converter weighted efficiency has been published for use in DCM operation, whereas in [29] the authors propose a control for an interleaved flyback converter, in which, depending on the input power, one of the converters is entirely switched OFF to maximize efficiency.

In this paper, the flyback inverter operating in improved BCM (i-BCM) will be studied. For this mode of operation, analytical equations as a function of time will be derived. Compared to [24], where all the equations are defined as a function of the reference input current, the proposed analysis offers the advantage of the calculation of the average and RMS value of the current for each component as well as the power losses, which, as it will be shown, are proven to be a lot more complex than when in DCM, due to the variable switching frequency. After that, by applying an optimization algorithm, the design parameter values for the converter can be determined for maximum weighted efficiency. Since the converter will be operating in BCM, the power density is higher, making it more cost effective for manufacturing, which is a key feature of the ac-PV module technology. Finally, by deriving the analytical equations, it will be shown that the use of high frequency current sensors is not required and only input and output voltage sensors are needed to implement the control algorithm on an experimental prototype. This offers the added advantage of simpler and more robust control for BCM. Measuring high frequency switching current poses many issues due to the noise and the high sampling frequency required [36]. More specifically, in order to measure the primary or secondary winding current instant value, one of the following sensors can be used: a shunt resistance, a Hall Effect sensor or a current transformer. While the shunt resistance offers the highest bandwidth, the overall efficiency of the converter is reduced. Moreover, towards the direction of achieving low THD the switching times need to be exact, so the sampling frequency needs to be extremely high imposing the use of a pricier DSP controller or FPGA. Additionally, the low frequency filters which need to be implemented in order to suppress the noise during switching result to a measuring lag which also affect the overall THD.

II. FLYBACK CONVERTER IN BOUNDARY CONDUCTION MODE AS A GRID-CONNECTED CURRENT SOURCE INVERTER

In Fig. 1 the flyback inverter topology is presented. The semiconductor switch S_p is the converter main switch and is modulated in high frequency. The isolation is achieved by the high frequency transformer which has two identical secondary windings, each one operating during a utility grid half cycle. This is achieved by the sequential conduction of the two semiconductor switches S_1 and S_2 that are modulated in the utility grid frequency. The secondary windings diodes ensure the flyback operation of the converter. The ac current is

injected to the utility grid via a low pass filter.

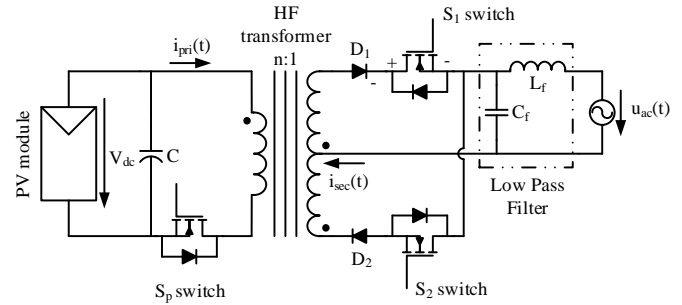


Fig. 1. Flyback inverter topology diagram.

The switching sequence of S_p can determine the mode of operation of the converter. For BCM, S_p must switch ON when the secondary winding current reaches zero and the transformer is completely demagnetized. The first time the BCM operation was presented for use in the ac-PV flyback current source inverter [19], the main transistor S_p ON time was determined in such a way that the peak input current followed a sinusoidal reference. As it will be demonstrated in the next section, this switching modulation technique provided a non sinusoidal output current, leading to a non optimal THD. However, for the improved BCM technique [24]-[25], the ON time in each switching cycle is determined in such a way that the ac output current to have the lowest possible THD, as demonstrated in the next paragraph. The switching sequence of each semiconductor is presented in Fig. 2.

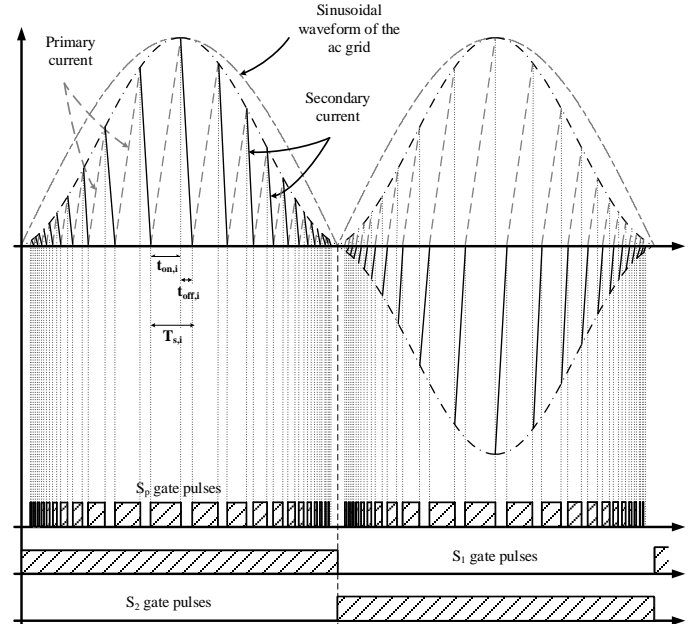


Fig. 2. Current waveforms and switching sequence diagram for i-BCM.

III. ANALYTICAL EQUATIONS DERIVATION FOR BCM

In this section, the analytical equations that describe the i-BCM operation are presented. Firstly, in order to achieve low THD, the appropriate switching modulation, as a function of time will be shown. Secondly, the average and RMS values of the input and output currents will be calculated.

A. Determination of the main switch modulation

As, it was described above, contrary to DCM, BCM has not a constant switching period, therefore:

$$T_{s,i}(t) = t_{on,i}(t) + t_{off,i}(t), \quad 0 \leq i \leq m \quad (1)$$

where m is the number of switching cycles during half the period of the ac utility grid.

For this analysis, it is considered that the grid voltage is sheer sinusoidal and that the switching frequency of S_p is a lot higher than the mains frequency, so as to be assumed that the grid voltage during each switching cycle remains constant and equal to the value at the beginning of the switching cycle:

$$V_{ac,i} = V_{acp} \sin(\omega t_{i-1}). \quad (2)$$

Therefore, the primary winding current, which is equal to the main switch current, is:

$$i_{pri}(t) = \frac{V_{dc}}{L_1} (t - t_{i-1}), \quad t_{i-1} \leq t \leq t_{i-1} + t_{on,i}. \quad (3)$$

The peak value of this current during each switching cycle is:

$$I_{pri,p,i} = \frac{V_{dc}}{L_1} t_{on,i} \quad (4)$$

and the peak value of the secondary winding current during each switching cycle is:

$$I_{sec,p,i} = n I_{pri,p,i} = \frac{V_{ac,i}}{\frac{L_1}{n^2}} t_{off,i}. \quad (5)$$

Based on the equations (2)-(5) we obtain:

$$t_{off,i} = \frac{\lambda}{n} \frac{t_{on,i}}{\sin(\omega t_{i-1})} \quad (6)$$

where:

$$\lambda = \frac{V_{dc}}{V_{acp}}. \quad (7)$$

The average value of the secondary winding current during each cycle is:

$$I_{sec,avg,i} = \frac{1}{T_{s,i}} \frac{n \frac{V_{dc}}{L_1} t_{on,i} t_{off,i}}{2} = \frac{\lambda V_{dc}}{2L_1} \frac{t_{on,i}^2}{T_{s,i} \sin(\omega t_{i-1})}. \quad (8)$$

The peak value of equation (8) is found at $\omega t = 90^\circ$, so:

$$I_{sec,avg,p} = \frac{\lambda V_{dc}}{2L_1} \frac{t_{on,p}^2}{T_{s,p}}. \quad (9)$$

In order to have the lowest possible THD for the output current, as well as for it to be in phase with the voltage of the utility grid, the average value of the secondary winding current during each switching cycle must have a sinusoidal form [37], therefore:

$$I_{sec,avg,i} = I_{sec,avg,p} \sin(\omega t_{i-1}). \quad (10)$$

Taking into consideration (2), (6), (8)-(10) we conclude that:

$$t_{on,i} = \frac{t_{on,p}}{1 + \frac{\lambda}{n}} \sin \omega t_{i-1} \left(\sin(\omega t_{i-1}) + \frac{\lambda}{n} \right), \quad 0 \leq \omega t_{i-1} \leq \pi \quad (11)$$

$$t_{off,i} = \frac{\frac{\lambda}{n}}{1 + \frac{\lambda}{n}} t_{on,p} \left(\sin(\omega t_{i-1}) + \frac{\lambda}{n} \right) \quad (12)$$

$$T_{s,i} = t_{on,i} + t_{off,i} = \frac{t_{on,p}}{1 + \frac{\lambda}{n}} \left(\sin(\omega t_{i-1}) + \frac{\lambda}{n} \right)^2. \quad (13)$$

The above equations are in accordance with the equations derived in [24]. However, the benefit of having the analytical equations as a function of time, and not as a function of a peak input current facilitates the calculation of the average and RMS values for a half time period of all the components currents. This will enable the designer to predict the power losses of the semiconductor devices and the transformer and to properly select the design parameters. These equations describe the exact switching modulation of S_p in order to achieve low THD. In the original BCM modulation [19], the primary winding current (as well as the main switch ON time) is considered to be sinusoidal. Based on this assumption, the average value of the secondary winding current during each switching cycle is:

$$I_{sec,avg,i} = \frac{\lambda V_{dc}}{2L_1} \frac{t_{on,p} \sin \omega t_{i-1}}{\left(\frac{\lambda}{n} + \sin \omega t_{i-1} \right)}. \quad (14)$$

If the value $\lambda/n \gg 1$, the output current is in fact sinusoidal, however if $\lambda/n < 1$, the output current becomes more like a square wave. The comparison between the output current for the presented switching modulation scheme and the original BCM modulation can be observed in Fig. 3.

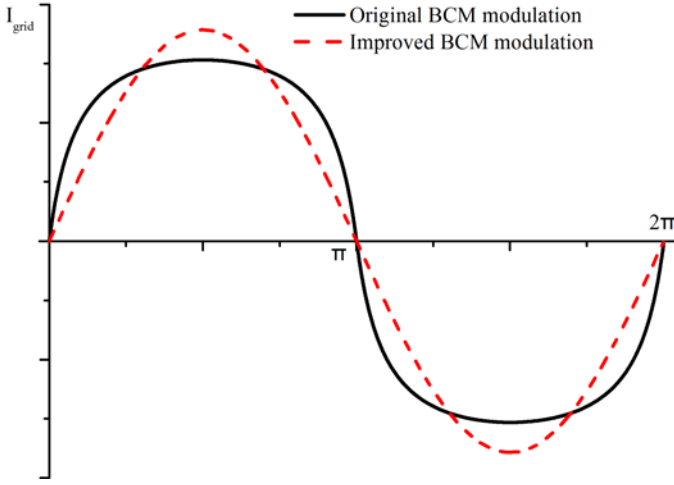


Fig. 3. Output current comparison between original and improved BCM operation.

B. Input and Output Current Calculation

It must be noted that, contrary to DCM, the switching frequency in i-BCM is not constant, so the derivation of the equations in this operating mode is significantly cumbersome and complex mathematical techniques and manipulations need to be implemented.

Beginning with the primary winding current, the average value can be determined with the following equation:

$$\begin{aligned} I_{\text{pri,avg}} &= \frac{1}{T_{\text{hl}}} \int_0^{T_{\text{hl}}} i_{\text{pri}}(t) dt = \frac{1}{T_{\text{hl}}} \sum_{i=0}^m \int_{t_{i-1}}^{t_i} i_{\text{pri}}(t) dt = \\ &= \frac{V_{\text{dc}}}{2L_1} \frac{1}{T_{\text{hl}}} \sum_{i=0}^m t_{\text{on},i}^2. \end{aligned} \quad (15)$$

Since m has a very large value:

$$T_{\text{hl}} \approx t_m = \sum_{i=0}^m T_{s,i} = \frac{t_{\text{on,p}}}{1 + \frac{\lambda}{n}} \sum_{i=0}^m \left(\frac{\lambda}{n} + \sin \left(\omega \sum_{j=0}^{i-1} T_{s,j} \right) \right). \quad (16)$$

Moreover, we can define:

$$\omega t_{i-1} = \omega \sum_{j=0}^{i-1} T_{s,j} = \theta_{i-1}. \quad (17)$$

Taking into account equations (1), (11), (17) and after some mathematical manipulations:

$$I_{\text{pri,avg}} = \frac{1}{2} \frac{V_{\text{dc}}}{L_1} \left(\frac{t_{\text{on,p}}}{1 + \frac{\lambda}{n}} \right)^2 \frac{\sum_{i=0}^m \sin^2 \theta_{i-1} \left(\sin \theta_{i-1} + \frac{\lambda}{n} \right)^2}{\frac{t_{\text{on,p}}}{1 + \frac{\lambda}{n}} \sum_{i=0}^m \left(\frac{\lambda}{n} + \sin \theta_{i-1} \right)^2}$$

$$\begin{aligned} &= \frac{1}{2} \frac{V_{\text{dc}}}{L_1} \frac{t_{\text{on,p}}}{1 + \frac{\lambda}{n}} \left[\left(\frac{\lambda}{n} \right)^2 \frac{\sum_{i=0}^m \sin^2 \theta_{i-1}}{\sum_{i=0}^m \left(\frac{\lambda}{n} + \sin \theta_{i-1} \right)^2} \right. \\ &\quad \left. + 2 \frac{\lambda}{n} \frac{\sum_{i=0}^m \sin^3 \theta_{i-1}}{\sum_{i=0}^m \left(\frac{\lambda}{n} + \sin \theta_{i-1} \right)^2} + \frac{\sum_{i=0}^m \sin^4 \theta_{i-1}}{\sum_{i=0}^m \left(\frac{\lambda}{n} + \sin \theta_{i-1} \right)^2} \right] \quad (18) \\ &= \frac{1}{2} \frac{V_{\text{dc}}}{L_1} \frac{t_{\text{on,p}}}{1 + \frac{\lambda}{n}} \Sigma I_{\text{pri,avg}} \\ &= \frac{1}{4} \frac{V_{\text{dc}}}{L_1} \frac{t_{\text{on,p}}}{1 + \frac{\lambda}{n}} \end{aligned}$$

since

$$\Sigma I_{\text{pri,avg}} = \frac{1}{2} \quad (19)$$

according to the analytical calculation presented in Appendix A.

The RMS value of the primary winding current can be found from the following equation:

$$\begin{aligned} I_{\text{pri,rms}}^2 &= \frac{1}{T_{\text{hl}}} \int_0^{T_{\text{hl}}} i_{\text{pri}}^2(t) dt = \frac{1}{T_{\text{hl}}} \sum_{i=0}^m \int_{t_{i-1}}^{t_i} i_{\text{pri}}^2(t) dt = \\ &= \frac{1}{3} \frac{1}{T_{\text{hl}}} \left(\frac{V_{\text{dc}}}{L_1} \right)^2 \sum_{i=0}^m t_{\text{on},i}^3. \end{aligned} \quad (20)$$

Taking into consideration equations (1), (11), (17):

$$\begin{aligned} I_{\text{pri,rms}}^2 &= \frac{1}{3} \frac{\left(\frac{V_{\text{dc}}}{L_1} \right)^2 \left(\frac{t_{\text{on,p}}}{1 + \frac{\lambda}{n}} \right)^3 \sum_{i=0}^m \left[\sin \theta_{i-1} \left(\sin \theta_{i-1} + \frac{\lambda}{n} \right) \right]^3}{\frac{t_{\text{on,p}}}{1 + \frac{\lambda}{n}} \sum_{i=0}^m \left(\frac{\lambda}{n} + \sin \theta_{i-1} \right)^2} \\ &= \frac{1}{3} \left(\frac{V_{\text{dc}}}{L_1} \right)^2 \left(\frac{t_{\text{on,p}}}{1 + \frac{\lambda}{n}} \right)^2 \frac{\sum_{i=0}^m \left[\sin \theta_{i-1} \left(\sin \theta_{i-1} + \frac{\lambda}{n} \right) \right]^3}{\sum_{i=0}^m \left[\frac{\lambda}{n} + \sin \theta_{i-1} \right]^2} \\ &= \left(\frac{n V_{\text{dc}}}{L_1} \right)^2 t_{\text{on,p}}^2 \frac{1}{6} \frac{\frac{\lambda}{n}}{\left(1 + \frac{\lambda}{n} \right)^2}. \end{aligned}$$

$$\begin{aligned}
 & \left[\left(\frac{\lambda}{n} \right)^3 \frac{\sum_{i=0}^m \sin^2 \theta_{i-1}}{\sum_{i=0}^m \left(\frac{\lambda}{n} + \sin \theta_{i-1} \right)^2} + 3 \left(\frac{\lambda}{n} \right)^2 \frac{\sum_{i=0}^m \sin^3 \theta_{i-1}}{\sum_{i=0}^m \left(\frac{\lambda}{n} + \sin \theta_{i-1} \right)^2} \right. \\
 & \left. + 3 \left(\frac{\lambda}{n} \right) \frac{\sum_{i=0}^m \sin^4 \theta_{i-1}}{\sum_{i=0}^m \left(\frac{\lambda}{n} + \sin \theta_{i-1} \right)^2} + \frac{\sum_{i=0}^m \sin^5 \theta_{i-1}}{\sum_{i=0}^m \left(\frac{\lambda}{n} + \sin \theta_{i-1} \right)^2} \right] \\
 & = \left(\frac{nV_{dc}}{L_1} \right)^2 t_{on,p}^2 \frac{1}{6} \frac{\frac{\lambda}{n}}{\left(1 + \frac{\lambda}{n} \right)^2} \Sigma I_{pri,rms} \\
 & = \frac{1}{3} \left(\frac{V_{dc}}{L_1} \right)^2 \left(\frac{t_{on,p}}{1 + \frac{\lambda}{n}} \right)^2 \left[\frac{3}{8} + \frac{4}{3\pi} \left(\frac{\lambda}{n} \right) \right] \quad (21)
 \end{aligned}$$

since

$$\Sigma I_{pri,rms} = \frac{3}{8} + \frac{4}{3\pi} \left(\frac{\lambda}{n} \right) \quad (22)$$

according to the analytical calculation presented in Appendix A.

Next, for the secondary winding, based on (3), the current equation during each switching cycle is:

$$i_{sec}(t) = nI_{pri,p,i} \left(1 - \frac{t - t_{i-1}}{t_{off,i}} \right), \quad t_{i-1} + t_{on,i} \leq t \leq t_{i-1} + t_{on,i} + t_{off,i} \quad (23)$$

So, the average current of the secondary winding, which is equal to the current of each secondary switch and diode, is:

$$\begin{aligned}
 I_{sec,avg} & = \frac{\sum_{i=0}^m I_{sec,avg,i}}{T_{hl}} \\
 & = \frac{\lambda V_{dc}}{4L_1} \frac{t_{on,p}}{1 + \frac{\lambda}{n}} \frac{\sum_{i=0}^m \left[\sin \theta_{i-1} \left(\sin \theta_{i-1} + \frac{\lambda}{n} \right)^2 \right]}{\sum_{i=0}^m \left[\frac{\lambda}{n} + \sin \theta_{i-1} \right]^2} \\
 & = \frac{\lambda V_{dc}}{4L_1} \frac{t_{on,p}}{1 + \frac{\lambda}{n}} \left[\left(\frac{\lambda}{n} \right)^2 \frac{\sum_{i=0}^m \sin \theta_{i-1}}{\sum_{i=0}^m \left[\frac{\lambda}{n} + \sin \theta_{i-1} \right]^2} \right. \\
 & \left. + 2 \frac{\lambda}{n} \frac{\sum_{i=0}^m \sin^2 \theta_{i-1}}{\sum_{i=0}^m \left[\frac{\lambda}{n} + \sin \theta_{i-1} \right]^2} + \frac{\sum_{i=0}^m \sin^3 \theta_{i-1}}{\sum_{i=0}^m \left[\frac{\lambda}{n} + \sin \theta_{i-1} \right]^2} \right]
 \end{aligned}$$

$$\begin{aligned}
 & = \frac{\lambda V_{dc}}{4L_1} \frac{t_{on,p}}{1 + \frac{\lambda}{n}} \Sigma I_{sec,avg} \quad (24) \\
 & = \frac{\lambda V_{dc}}{2\pi L_1} \frac{t_{on,p}}{1 + \frac{\lambda}{n}}
 \end{aligned}$$

since

$$\Sigma I_{sec,avg} = \frac{2}{\pi} \quad (25)$$

according to the analytical calculation presented in Appendix A.

Finally, the secondary winding current RMS value can be calculated by:

$$\begin{aligned}
 I_{sec,rms}^2 & = \frac{1}{2T_{hl}} \sum_{i=0}^m \int_{t_{i-1}}^{t_i} i_{sec}^2(t) dt \\
 & = \frac{1}{2T_{hl}} \sum_{i=0}^m \int_{t_{i-1} + t_{on,i}}^{t_{i-1} + t_{off,i}} (nI_{pri,p,i})^2 \left(1 - \frac{t - t_{i-1}}{t_{off,i}} \right)^2 dt \\
 & = \left(\frac{nV_{dc}}{L_1} \right)^2 \frac{t_{on,p}^3}{6T_{hl}} \frac{\frac{\lambda}{n}}{\left(1 + \frac{\lambda}{n} \right)^3} \frac{n^2 t_{off}^2}{3} \\
 & \cdot \sum_{i=0}^m \left[\sin^2(\omega t_{i-1}) \left(\frac{\lambda}{n} + \sin(\omega t_{i-1}) \right)^3 \right] \\
 & = \left(\frac{nV_{dc}}{L_1} \right)^2 t_{on,p}^2 \frac{1}{6} \frac{\frac{\lambda}{n}}{\left(1 + \frac{\lambda}{n} \right)^2} \\
 & \cdot \left[\left(\frac{\lambda}{n} \right)^3 \frac{\sum_{i=0}^m \sin^2 \theta_{i-1}}{\sum_{i=0}^m \left(\frac{\lambda}{n} + \sin \theta_{i-1} \right)^2} + 3 \left(\frac{\lambda}{n} \right)^2 \frac{\sum_{i=0}^m \sin^3 \theta_{i-1}}{\sum_{i=0}^m \left(\frac{\lambda}{n} + \sin \theta_{i-1} \right)^2} \right. \\
 & \left. + 3 \left(\frac{\lambda}{n} \right) \frac{\sum_{i=0}^m \sin^4 \theta_{i-1}}{\sum_{i=0}^m \left(\frac{\lambda}{n} + \sin \theta_{i-1} \right)^2} + \frac{\sum_{i=0}^m \sin^5 \theta_{i-1}}{\sum_{i=0}^m \left(\frac{\lambda}{n} + \sin \theta_{i-1} \right)^2} \right] \\
 & = \left(\frac{nV_{dc}}{L_1} \right)^2 t_{on,p}^2 \frac{1}{6} \frac{\frac{\lambda}{n}}{\left(1 + \frac{\lambda}{n} \right)^2} \Sigma I_{sec,rms} \\
 & = \left(\frac{nV_{dc}}{L_1} \right)^2 t_{on,p}^2 \frac{1}{6} \frac{\frac{\lambda}{n}}{\left(1 + \frac{\lambda}{n} \right)^2} \left(\frac{1}{2} \frac{\lambda}{n} + \frac{4}{3\pi} \right) \quad (26)
 \end{aligned}$$

since

$$\Sigma I_{\text{sec,rms}} = \frac{1}{2} \frac{\lambda}{n} + \frac{4}{3\pi} \quad (27)$$

according to the analytical calculation presented in Appendix A.

IV. CALCULATION OF COMPONENT LOSSES FOR THE I-BCM OPERATION

Having calculated the average and RMS values of the transformer input and output current, the power losses of the flyback inverter operated in i-BCM can be quantified. These losses can be distinguished in two types: semiconductor losses and transformer losses.

A. Semiconductor losses

The semiconductor losses are separated into conduction losses and switching losses.

The conduction losses of the switching devices, assuming that MOSFETs are used, are:

For S_p :

$$P_{CL,SW,pri} = I_{pri,rms}^2 R_{ds,pri} \quad (28)$$

Since there are two switches S_1 and S_2 on the secondary transformer side:

$$P_{CL,SW,sec} = 2 \cdot I_{sec,rms}^2 R_{ds,sec} \quad (29)$$

Assuming that the diode resistance is negligible, the conduction losses for the diodes are:

$$P_{CL,d} = 2 \cdot I_{sec,avg} V_d \quad (30)$$

Since the goal of the optimization procedure is to define the converter design parameters and the transformer ratio n is one of those parameters, the primary switch peak voltage varies during the optimization algorithm and, as a result, depending on this breakdown voltage, the appropriate MOSFET needs to be selected. However, the ON resistance $R_{ds,on}$ of the switch is a function of this breakdown voltage [38], and it can be estimated using the following equation:

$$R_{ds,on} = k_1 (V_{tr,BD})^{k_2} + k_3 \quad (31)$$

The parameters k_1 , k_2 and k_3 depend on the fabrication technology as well as the switch package. Therefore, after diligently studying different MOSFETs found on the market and by using curve fitting, the parameters that were used during the optimization procedure are shown in Table I.

As S_1 , S_2 are switched ON at zero voltage and switched OFF at zero current and S_p is switched ON at zero current, all the switching losses can be neglected, except the switching losses during the turn OFF transition of S_p . So the switching losses during each cycle are:

$$E_i = \frac{V_{sp,i} \cdot I_{sp,i}}{2} t_{f,pri} = \frac{V_{sp,i} \cdot I_{pri,p,i}}{2} t_{f,pri} \quad (32)$$

Since the switching frequency is much higher than the frequency of the grid we can assume that the voltage across the semiconductor device during the switching time remains constant and equal to:

$$V_{sp,i} = V_{dc} + nV_{acp} \sin(\omega t_{i-1}) \quad (33)$$

By combining (4) and (33), equation (32) can be rewritten as:

$$E_i = \frac{t_{f,pri} V_{dc}^2 t_{on,p}}{2L_1 \left(1 + \frac{\lambda}{n}\right)} \left[\frac{\lambda}{n} \sin(\omega t_{i-1}) + 2 \sin^2(\omega t_{i-1}) + \frac{1}{\frac{\lambda}{n}} \sin^3(\omega t_{i-1}) \right] \quad (34)$$

In order to calculate the power loss for a time period of T_{hl} we can write:

$$P_{SL,SW,pri} = \frac{1}{T_{hl}} \sum_{i=1}^m E_i = \frac{t_{f,pri} V_{dc}^2}{2L_1} \left[\left(\frac{\lambda}{n}\right) \frac{\sum_{i=0}^m \sin(\omega t_{i-1})}{\sum_{i=0}^m \left(\frac{\lambda}{n} + \sin \theta_{i-1}\right)^2} + 2 \frac{\sum_{i=0}^m \sin^2(\omega t_{i-1})}{\sum_{i=0}^m \left(\frac{\lambda}{n} + \sin \theta_{i-1}\right)^2} + \frac{1}{\left(\frac{\lambda}{n}\right)} \frac{\sum_{i=0}^m \sin^3(\omega t_{i-1})}{\sum_{i=0}^m \left(\frac{\lambda}{n} + \sin \theta_{i-1}\right)^2} \right] \quad (35)$$

$$= \frac{t_{f,pri} V_{dc}^2}{2L_1} \Sigma P_{SL,SW,pri} = \frac{t_{f,pri} V_{dc}^2}{L_1} \frac{1}{\frac{\lambda}{n} \pi}$$

since

$$\Sigma P_{SL,SW,pri} = \frac{2}{\frac{\lambda}{n} \pi} \quad (36)$$

according to the analytical calculations presented in Appendix B.

B. Transformer Losses

The transformer losses can also be separated into two categories: core losses P_{CRL} and copper (windings) losses P_{CuL} . There are several models and formulas for core losses for nonsinusoidal flux waveforms (as the ones that are usually found in power electronics converters): hysteresis models, such as Preisach [39] and Jiles/Atherton [40], models based on loss separation [41] or empirical formulas, such as different

TABLE I
MOSFET ON RESISTANCE PARAMETERS

Breakdown Voltage Range	LOW VOLTAGE (<400V)			HIGH VOLTAGE (>400V)		
Package	k ₁	k ₂	k ₃	k ₁	k ₂	k ₃
PLUS247	2.39·10 ⁻⁸	2.4	0.005789	1.898·10 ⁻⁸	2.4	0
PLUS 264	1.506·10 ⁻⁸	2.4	0.004919	1.389·10 ⁻⁸	2.4	0
TO247	5.2916·10 ⁻⁸	2.48	0.01	3.355·10 ⁻⁸	2.417	0
TO264	2.327·10 ⁻⁸	2.4	0.006336	6.833·10 ⁻⁹	2.558	0

versions of the Steinmetz equation [42]-[44]. For the core loss estimation of the flyback inverter, the improved generalized Steinmetz equation (iGSE) [44] was applied. According to iGSE, the core losses during a switching period of any arbitrary waveform are:

$$P_{CRL,i} = V_e \frac{k_f (\Delta B)^{\beta-\alpha}}{T} \sum_j \left| \frac{V_j(t_j)}{N_{pri} A_e} \right|^\alpha (\Delta t_j) \quad (37)$$

where:

$$k_f = \frac{k}{2^{\beta+1} \pi^{\alpha-1} \left(0.2761 + \frac{1.7061}{\alpha+1.354} \right)} \quad (38)$$

The parameters α , β , k depend on the core material used.

In order to apply the equation over the flyback converter electrical conditions, the magnetic flux fluctuation must be calculated. The excitation of the transformer is shown in Fig. 4 and is described by the following equation:

$$V_j(t_i) = \begin{cases} V_{dc} & , t_{i-1} \leq t \leq t_{i-1} + t_{on,i} \\ -nV_{ac}(\omega(t_{i-1} + t_{on,i})) & , t_{i-1} + t_{on,i} \leq t \leq t_{i-1} + t_{on,i} + t_{off,i} \end{cases} \quad (39)$$

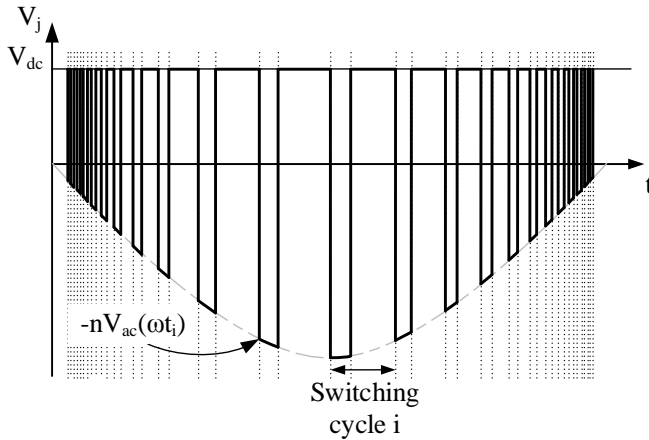


Fig. 4. Voltage across the high frequency transformer.

and since for the flyback inverter:

$$\Delta B_i = \frac{V_{dc} t_{on,i}}{N_{pri} A_e} \quad (40)$$

the core losses during each switching cycle are:

$$P_{CRL,i} = V_e \frac{k_f \Delta B_i^{\beta-\alpha}}{T_{s,i}} \cdot \left[\left(\frac{V_{dc}}{N_{pri} A_e} \right)^\alpha t_{on,i} + \left(\frac{n}{N_{pri} A_e} \cdot V_{ac}(\omega(t_{i-1} + t_{on,i})) \right)^\alpha \cdot t_{off,i} \right] \quad (41)$$

Taking into consideration (40), (11), (12):

$$P_{CRL,i} = V_e \frac{k_f}{T_{s,i}} \left(\frac{V_{dc}}{N_{pri} A_e} \right)^\beta \left[\frac{t_{on,p}}{1 + \frac{\lambda}{n}} \sin \omega t_{i-1} (\sin(\omega t_{i-1}) + \frac{\lambda}{n})^{\beta-\alpha+1} \cdot \left[1 + \left(\frac{n}{\lambda} \sin(\omega t_{i-1}) \right)^{\alpha-1} \right] \right] \quad (42)$$

The total core losses are found by averaging the core losses during each switching cycle:

$$P_{CRL} = \frac{1}{T_{hl}} \sum_{i=1}^m T_{s,i} P_{CRL,i} = V_e k_f \left(\frac{V_{dc}}{N_{pri} A_e} \right)^\beta \left[\frac{t_{on,p}}{1 + \frac{\lambda}{n}} \right]^{\beta-\alpha} \frac{\sum_{i=0}^m \left[\left(\sin \theta_{i-1} + \frac{\lambda}{n} \right)^{\beta-\alpha+1} \right]}{\left[\sum_{i=0}^m \left(\frac{\lambda}{n} + \sin \theta_{i-1} \right)^2 \right]} \cdot \frac{\left[(\sin \theta_{i-1})^{\beta-\alpha+1} + \left(\frac{n}{\lambda} \right)^{\alpha-1} (\sin \theta_{i-1})^\beta \right]}{\left[\sum_{i=0}^m \left(\frac{\lambda}{n} + \sin \theta_{i-1} \right)^2 \right]} \quad (43)$$

As (43) cannot be directly solved, the analytical equation has been derived by applying curve fitting techniques and linear approximation using mathematical software [45]. So, the core losses for i-BCM are approximated by:

$$P_{CRL} = V_e k_f \left(\frac{V_{dc}}{N_{pri} A_e} \right)^\beta \left(\frac{t_{on,p}}{1 + \frac{\lambda}{n}} \right)^{\beta-\alpha} \cdot Q \left(\alpha, \beta, \frac{\lambda}{n} \right) \quad (44)$$

where:

$$Q \left(\alpha, \beta, \frac{\lambda}{n} \right) \approx \frac{1}{\sqrt{\pi}} \left(\frac{\lambda}{n} \right)^{-2\alpha+\beta} \left[\frac{Gm \left[\frac{1+\beta}{2} \right] Y\Gamma \left[\left\{ \frac{1+\alpha-\beta}{2}, 1+\frac{\alpha-\beta}{2}, \frac{1+\beta}{2} \right\} \right]}{Gm \left[1+\frac{\beta}{2} \right]} \right. \\ \left. \cdot \frac{\left\{ \frac{1}{2}, 1+\frac{\beta}{2} \right\}, \frac{1}{\left(\frac{\lambda}{n} \right)^2}}{Gm \left[1+\frac{\beta}{2} \right]} + \frac{\left(\frac{\lambda}{n} \right)^{-1+\alpha} Gm \left[\frac{1}{2}(2-\alpha+\beta) \right]}{Gm \left[\frac{1}{2}(3-\alpha+\beta) \right]} \right] \\ \cdot Y\Gamma \left[\left\{ \frac{1+\alpha-\beta}{2}, 1+\frac{\alpha-\beta}{2}, 1-\frac{\alpha+\beta}{2} \right\}, \left\{ \frac{1}{2}, \frac{3-\alpha+\beta}{2} \right\}, \frac{1}{\left(\frac{\lambda}{n} \right)^2} \right] \\ \cdot \frac{(1+\alpha-\beta) Gm \left[1+\frac{\beta}{2} \right]}{\frac{\lambda}{n} Gm \left[\frac{3+\beta}{2} \right]} \\ \cdot Y\Gamma \left[\left\{ 1+\frac{\alpha-\beta}{2}, \frac{3+\alpha-\beta}{2}, 1+\frac{\beta}{2} \right\}, \left\{ \frac{3}{2}, \frac{3+\beta}{2} \right\}, \frac{1}{\left(\frac{\lambda}{n} \right)^2} \right] \\ \cdot \frac{\left(\frac{\lambda}{n} \right)^{-2+\alpha} (1+\alpha-\beta) Gm \left[\frac{1}{2}(3-\alpha+\beta) \right]}{Gm \left[\frac{1}{2}(4-\alpha+\beta) \right]} \\ \cdot Y\Gamma \left[\left\{ 1+\frac{\alpha-\beta}{2}, \frac{3+\alpha-\beta}{2}, \frac{3-\alpha+\beta}{2} \right\}, \left\{ \frac{3}{2}, 2-\frac{\alpha+\beta}{2} \right\}, \frac{1}{\left(\frac{\lambda}{n} \right)^2} \right] \quad (45)$$

and where $Y\Gamma[\]$ is the hypergeometric function and $Gm[\]$ is the gamma function.

The Copper losses are caused by ohmic resistance that varies due to the skin and proximity effect [46], [47], which are the result of high frequency current through the windings. In order to minimize these effects, litz wire with low diameter strands is used in high frequency transformers.

The transformer copper losses of the flyback converter can be calculated by:

$$P_{CuL,z} = R_{dc,z} I_{avg,z}^2 + \sum_{n=1}^{\infty} R_{ac,n,z} I_{rms,n,z}^2 \quad (46) \\ = R_{dc,z} I_{avg,z}^2 + R_{dc,z} \sum_{n=1}^{\infty} F_{r,n,z} I_{rms,n,z}^2$$

where n refers to the current harmonic order and z refers to the

transformer winding (primary or secondary). For the calculation of $F_{r,n,z}$ the method described in [48] is used. As the calculation of the current higher order harmonics is extremely cumbersome, the copper losses are estimated using the approximation proposed in [49], [50]:

$$P_{CuL,z} = R_{dc,z} I_{avg,z}^2 + R_{dc,z} F_{r,n,z} I_{rms,ac,z}^2 \quad (47)$$

where:

$$I_{rms,ac,z}^2 = I_{rms,z}^2 - I_{avg,z}^2 \quad (48)$$

The parameter $F_{r,n,z}$ is a function of the switching frequency, which in this case does not remain constant. As a result, the average switching frequency was used which is defined by the following equation:

$$f_{s,avg} = \frac{1}{T_{s,avg}} = \left(\sum_{i=0}^m \frac{T_{s,i}}{T_{h1}} \right)^{-1} = \left(\frac{\left(\frac{t_{on,p}}{1 + \frac{\lambda}{n}} \right)^2 \sum_{i=0}^m \left(\frac{\lambda}{n} + \sin \theta_{i-1} \right)^4}{\frac{t_{on,p}}{1 + \frac{\lambda}{n}} \sum_{i=0}^m \left(\frac{\lambda}{n} + \sin \theta_{i-1} \right)^2} \right)^{-1} \\ = \left\{ \frac{t_{on,p}}{1 + \frac{\lambda}{n}} \left[\left(\frac{\lambda}{n} \right)^4 \frac{1}{\sum_{i=0}^m \left(\frac{\lambda}{n} + \sin \theta_{i-1} \right)^2} + 4 \left(\frac{\lambda}{n} \right)^3 \right. \right. \\ \left. \left. \cdot \frac{\sum_{i=0}^m \sin \theta_{i-1}}{\sum_{i=0}^m \left(\frac{\lambda}{n} + \sin \theta_{i-1} \right)^2} + 6 \left(\frac{\lambda}{n} \right)^2 \frac{\sum_{i=0}^m \sin^2 \theta_{i-1}}{\sum_{i=0}^m \left(\frac{\lambda}{n} + \sin \theta_{i-1} \right)^2} \right. \right. \\ \left. \left. + 4 \frac{\lambda}{n} \frac{\sum_{i=0}^m \sin^3 \theta_{i-1}}{\sum_{i=0}^m \left(\frac{\lambda}{n} + \sin \theta_{i-1} \right)^2} + \frac{\sum_{i=0}^m \sin^4 \theta_{i-1}}{\sum_{i=0}^m \left(\frac{\lambda}{n} + \sin \theta_{i-1} \right)^2} \right] \right\}^{-1} \\ = \left(\frac{t_{on,p}}{1 + \frac{\lambda}{n}} \Sigma T_{s,avg} \right)^{-1} \\ = \frac{1}{t_{on,p}} \frac{1 + \frac{\lambda}{n}}{\left(\frac{\lambda}{n} \right)^2 + \frac{4}{\pi} \frac{\lambda}{n} + \frac{1}{2}} \quad (49)$$

since

$$\Sigma T_{s,avg} = \left(\frac{\lambda}{n} \right)^2 + \frac{4}{\pi} \frac{\lambda}{n} + \frac{1}{2} \quad (50)$$

according to the analytical calculation presented in Appendix C. Moreover, the following ratios, the calculation of which is also shown in Appendix C, demonstrate the effect of λ and n on the converter operation:

$$\frac{f_{s,\max}}{f_{s,\text{avg}}} = \frac{\left(\frac{\lambda}{n}\right)^2 + \frac{4\lambda}{\pi n} + \frac{1}{2}}{\left(\frac{\lambda}{n}\right)^2} \quad (51)$$

$$\frac{f_{s,\min}}{f_{s,\text{avg}}} = \frac{\left(\frac{\lambda}{n}\right)^2 + \frac{4\lambda}{\pi n} + \frac{1}{2}}{\left(1 + \frac{\lambda}{n}\right)^2}. \quad (52)$$

Additionally, power is lost due to the leakage inductance of the transformer. This energy is dissipated on the primary switch passive snubber. The percentage of the lost power is equal to the ratio of the leakage inductance divided by the primary inductance of the transformer and varies between 0.5% and 3% on laboratory prototypes [35]. In this paper it is considered that 2.4% of the power is lost due to leakage inductance, according to the in-house built transformer of the experimental prototype that was implemented.

V. WEIGHTED EFFICIENCY OPTIMIZATION

Due to the nature of photovoltaic energy, the input power of the converter is not always at its nominal value. In fact, the converters operate at 30%-80% of their nominal power during 80% of the time. As a result, a correct design should not aim to achieve the highest possible efficiency only at the maximum input power, but it should take into consideration and optimize the performance at several power levels which correspond to different irradiance levels. For this reason, the European weighted-efficiency [34], given by (53), and the American weighted-efficiency [34], given by (54) were established.

$$\eta_{EUR} = 0.03 \cdot \eta_{5\%} + 0.06 \cdot \eta_{10\%} + 0.13 \cdot \eta_{20\%} + 0.10 \cdot \eta_{30\%} + 0.48 \cdot \eta_{50\%} + 0.20 \cdot \eta_{100\%} \quad (53)$$

$$\eta_{CEC} = 0.04 \cdot \eta_{10\%} + 0.05 \cdot \eta_{20\%} + 0.12 \cdot \eta_{30\%} + 0.21 \cdot \eta_{50\%} + 0.53 \cdot \eta_{75\%} + 0.05 \cdot \eta_{100\%} \quad (54)$$

where η_w is the efficiency at a specified PV power level $P_{PV,w}$ given as a percentage of the nominal power $P_{PV,nom}$ of the PV module. So,

$$w(\%) = \frac{P_{PV,w}}{P_{PV,nom}} \cdot 100 \quad (55)$$

$$\eta_w = 1 - \frac{P_{loss,w}}{P_{PV,w}} = 1 - r_{loss,w} \quad (56)$$

where $P_{loss,w}$ are the inverter losses at the specified power level.

A. Design Methodology

Having derived the equations that describe the operation of the flyback inverter during i-BCM, as well as the power losses of each component, it is now possible to apply an optimization methodology during the selection of the system parameters. The aim of each optimization algorithm is to maximize an objective function. In this paper, the converter European weighted efficiency was selected. Special effort was given to limit the number of independent parameters of the optimization algorithm. Based on the derived equations and after some additional manipulations, the performance parameters are: n , $t_{on,p}$, J , B_p .

Firstly, the converter specifications have to be set, meaning the input power (the MPP of the PV module), the input voltage (maximum, minimum and nominal at MPP) and output grid voltage (RMS value and frequency). It should be noted that because of the variable conditions (solar insolation, temperature), the input voltage of the converter will not be constant when the converter operates at nominal power of the solar panel under MPPT conditions. Therefore, the design algorithm must be applied for the worst case of the application. The relation between the main semiconductor switch peak ON time $t_{on,p}$ and the input power, for any level is:

$$P_{PV,w} = I_{pri,avg} V_{dc} = \frac{1}{4} \frac{V_{dc}^2}{L_1} \frac{t_{on,p,w}}{1 + \frac{\lambda}{n}} \quad (57)$$

Secondly, the constraints of the optimization problem have to be defined. These limitations are described in the following equations and include: the secondary switches maximum voltage (58), the transformer maximum temperature rise (59) [51], the copper fill factor of the core window (60) [51] and the maximum flux density to avoid saturation (61). The analysis of those equations is thoroughly described in [35].

$$V_{tr,sec,\max}(n) = \left(\frac{1}{C_f} \frac{P_{PV,nom}}{2f_{s,avg} V_{acp}} \left(\frac{2nV_{acp} + V_{dc,\min}}{nV_{acp} + V_{dc,\min}} \right)^2 + 2V_{acp} \right) \cdot 130\% \leq V_{tr,BD} \quad (58)$$

$$DT(n, V_{dc}, t_{on,p}, B_p, J, r) = R_t [P_{CRL}(n, V_{dc}, t_{on,p}, B_p) + P_{CPL}(n, V_{dc}, t_{on,p}, B_p, J, r)] \leq DT_{\max} \quad (59)$$

$$C_{ff}(n, V_{dc}, t_{on,p}, B_p, J, r) = \frac{A_{w,Cu}(n, V_{dc}, t_{on,p}, B_p, J, r)}{A_w} \leq C_{ff,\max} \quad (60)$$

$$B_p \leq B_{sat} \quad (61)$$

Finally, since the design specifications and constrains are clearly defined, the optimization algorithm to minimize the power losses described in the previous section and maximize performance can now be applied. The flow chart of the optimization sequence is shown in Fig. 5. The process is implemented on a software platform [45] and the differential evolution stochastic method for constrained nonlinear global optimization is used. The objective function to be optimized is (53), which is calculated based on (28), (29), (30), (35) and

(44), (47) for the semiconductor losses and the transformer losses respectively. This process is possible since the equations for the average and RMS currents were analytically derived in Section III. The optimization method is executed in order to determine a converter design according to the specifications provided by the user as well as the constraints, described in (58)-(61). This sequence is iterated for every possible transformer core and each time, the independent optimization variables n , $t_{on,p}$, B_p , J are determined and based on those, the corresponding efficiencies are calculated. If there is no acceptable design according to the specifications, then the material parameters (MOSFET package type, litz wire strand radius) need to be revised. On the other hand, if a design which satisfies the volume requirement is found, then the remaining design parameters (dependent variables) shown in Table II are calculated, based on the independent variables. The algorithm indicates the minimum breakdown voltage and maximum $R_{ds,on}$ for each MOSFET and so the MOSFET types are selected in order to satisfy those values. The same sequence is performed for the diodes.

density and temperature rise. In this paper, Power MOSFETs with a PLUS247 package were used. All of the design parameters of the implemented prototype, meaning the independent variables derived by the optimization algorithm, as well as the dependent variables are shown in Table II. The weighted efficiency for different operating conditions is shown in Table III.

TABLE II
INVERTER DESIGN PARAMETERS

Specifications and constraints	Independent variables	Dependent variables
$V_{dc,min}=31V$ $V_{dc,max}=40V$ $P_{PV,max}=205W$ grid: 230V/50Hz Core Material: 3f3	$n=0.132$ $t_{on,p,max}=41.16\mu s$ $B_p=280mT$ $J=5.1A/mm^2$	S_p : IXFX180N15 S_{I1}, S_{I2} : IXFX26N120 Diode: RHR15120 $r=0.15mm$ $str_{pri}=29$ $str_{sec}=3$ $N_{pri}=21, (L_l=41.2\mu H)$ $l_g=0.377cm$ Core Type: ETD54 $C_f=386nF$ $L_f=10mH$
$V_{tr,BD}=1200V$ $DT_{max}=85^\circ C$ $C_{ff,max}=35\%$ $B_{sat}=280mT$		

TABLE III
CALCULATED EUROPEAN EFFICIENCY

Maximum Power	Input Voltage	Calculated Weighted-Efficiency (%)
205W	40V	91.59
180W	36V	91.38
140W	31V	91.51

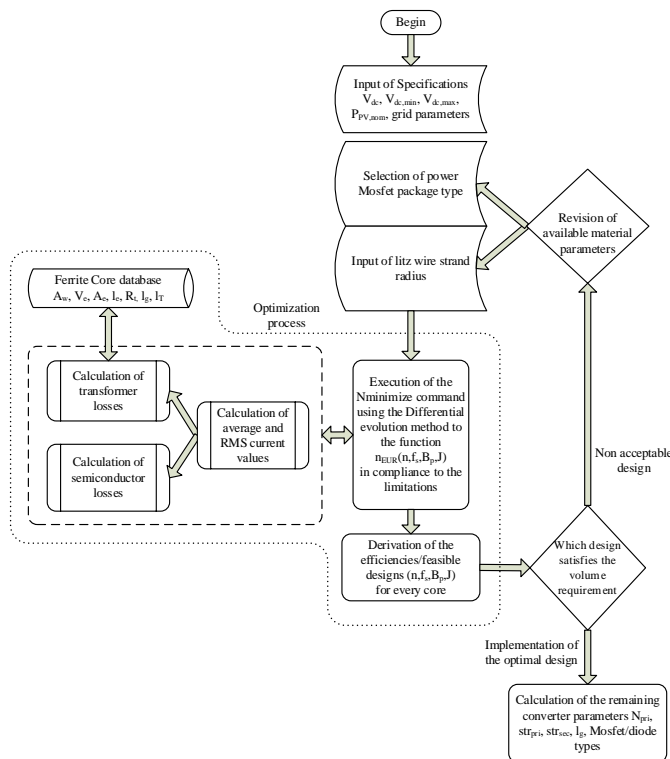


Fig. 5. Flow chart of the optimization sequence.

B. Optimization Example

In order to validate the above, the design methodology was applied for a flyback inverter operated in i-BCM for connection to the European utility grid, powered by a mono-crystalline 72-cell panel, which has a nominal power of 180W at STC. The operating temperature limits were selected to be 0°C and 60°C. The optimization algorithm was applied for the worst case, which in the current example is for 0°C, as in this temperature the PV module outputs its maximum power at its maximum voltage, leading to the highest component current and voltage stress as well as highest transformer core flux

Since the power losses of each component were calculated separately, the effect of each component on the converter efficiency can be observed for different input power. Fig. 6 shows the allocation of the power losses between the semiconductor devices and the transformer. In Figs. 7-8 those power losses are broken down further. The percentage of the semiconductor switches conduction losses is proportional to the input power whereas the S_p switching losses diminish as the input power increases. This is due to the nature of the i-BCM switching modulation. As the input power increases, the switching frequency decreases, reducing the effect of the switching losses. On the other hand, the input and output power increases, raising the conduction losses. Likewise, the transformer windings losses decrease, as they are a function of the switching frequency as well, having a minimum at about 35%, but for higher input power they increase again because of the higher currents. The losses due to the dissipation of the energy stored in leakage inductance remain constant and independent of the input power.

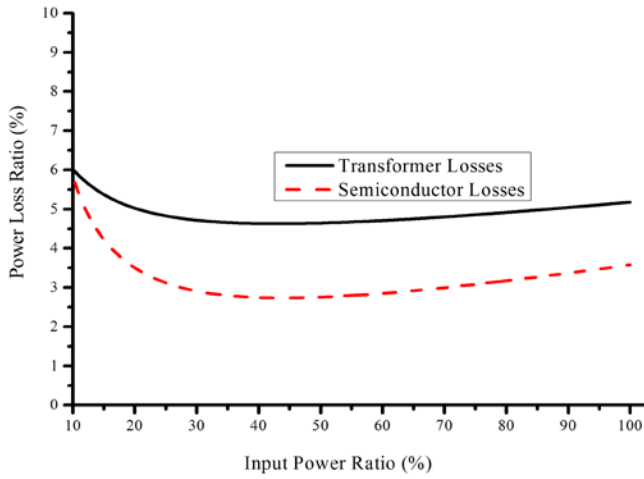


Fig. 6. Power losses of the two main components ($V_{dc} = 40V$).

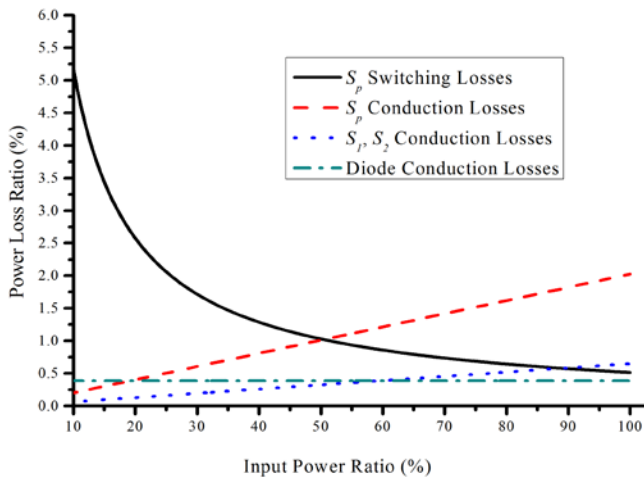


Fig. 7. Semiconductors losses analysis ($V_{dc} = 40V$).

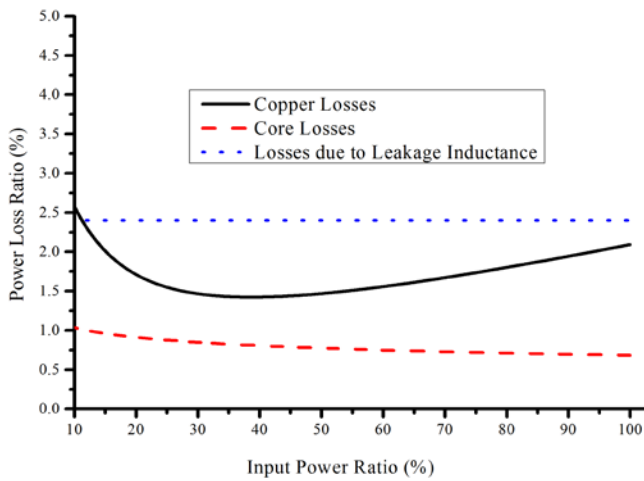


Fig. 8. Transformer losses analysis ($V_{dc} = 40V$).

VI. EXPERIMENTAL RESULTS

A flyback converter prototype, shown in Fig. 9, was implemented in order to verify the analysis, using the design parameters of Table II. A constant DC voltage source was used to emulate the PV panel. The modulation of the

semiconductor switches is performed by the dsPIC30f4011 microcontroller. The pulses for the S_1 , S_2 switches are generated based on the polarity of the sampled ac grid voltage. The converter input voltage is also sampled and together with the grid voltage, the primary semiconductor switch S_p is modulated, by implementing equations (11), (12), so no high frequency current sensors are needed. The converter input and output current at maximum power are shown in Fig. 10 and Fig. 11 respectively. The harmonic spectrum of the output current for maximum power can be observed in Fig. 12. The THD of the output current is 3.77%.

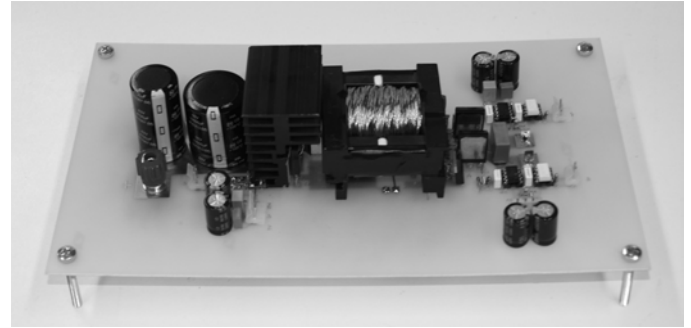


Fig. 9. Experimental prototype.

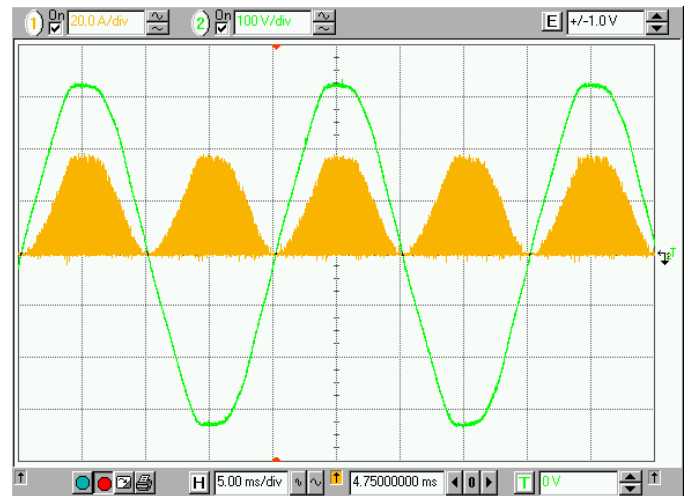


Fig. 10. Transformer primary winding current and grid voltage (20A/div, 100V/div, 5ms/div).

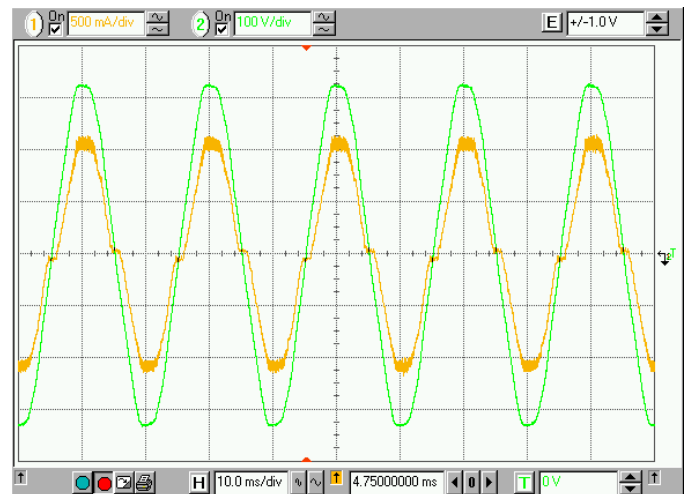


Fig. 11. Converter output current and grid voltage (0.5A/div, 100V/div, 10ms/div).

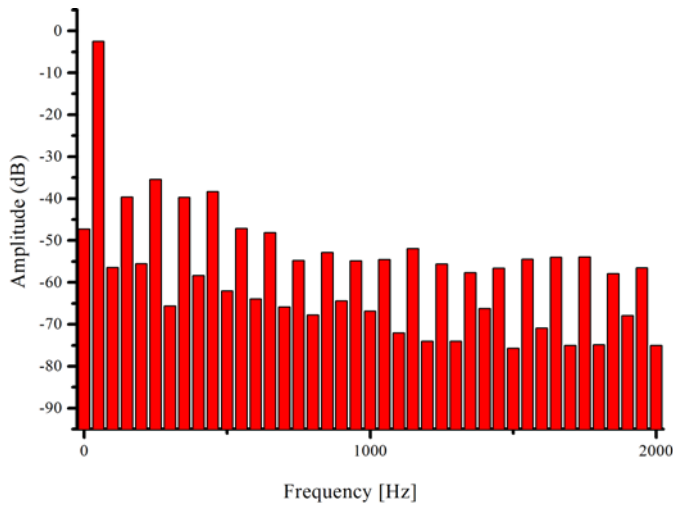


Fig. 12. Converter output current harmonic spectrum.

For the verification of the power loss analysis under i-BCM operation, the precision power analyzer LMG500 of ZES Zimmer manufacturer was used to conduct precise power measurements. The comparison between the measured efficiency and the predicted efficiency based on the power loss analysis equations, for different input voltages, is shown in Figs. 13-15.

Although the presented formulas are an estimation of the power losses of each converter component, the good correlation between the efficiency of the experimental results and the efficiency predicted by the optimization algorithm validates the power loss analysis calculations. As shown in the previous section, there is a global minimum of the power losses around the 35% of the maximum input power ratio. Because of the variable switching frequency used in the i-BCM modulation, for lower power levels, the switching frequency reaches very high values, dropping the converter efficiency, whereas for higher power levels, the converter efficiency slightly drops as well, because of the higher currents. The same behavior occurs for the three different input voltages.

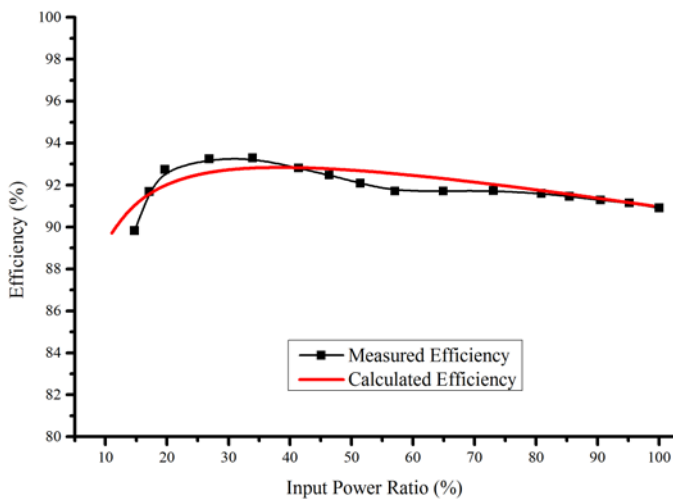


Fig. 13. Calculated and measured efficiency versus power ratio for $V_{dc} = 40V$.

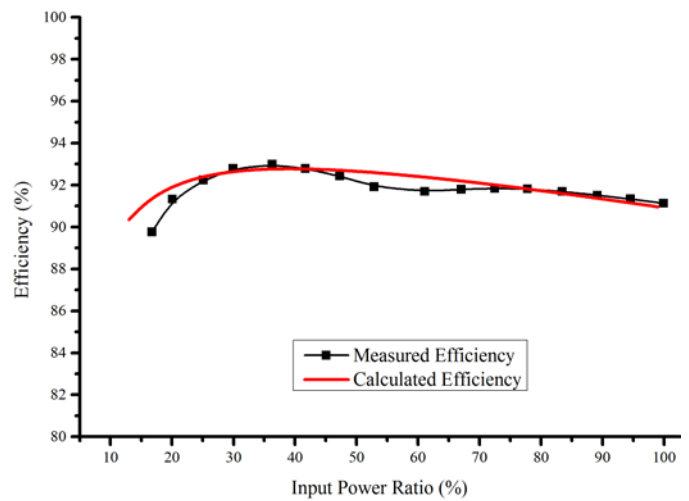


Fig. 14. Calculated and measured efficiency versus power ratio for $V_{dc} = 36V$.

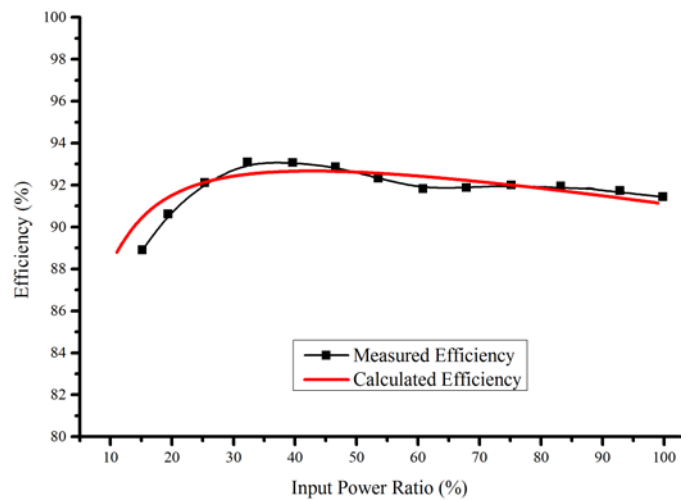


Fig. 14. Calculated and measured efficiency versus power ratio for $V_{dc} = 31V$.

The power circuit of the converter under optimization consists of a minimum number of power components, two diodes and three gate controlled semiconductors. The reduced complexity of the power topology offers high reliability and low cost but also due to the optimization methodology high levels of efficiency can be achieved. Specifically, the efficiency performance of the prototype inverter, for the power levels that the PV panel operates most frequently (higher weights in the European efficiency equation), the efficiency of the implemented converter is over 92% and the European efficiency is about 91.5%. However, it should be mentioned that this is an experimental laboratory prototype which is used to validate the mathematical analysis. A significant amount of the power losses is due to the leakage inductance of the transformer, the energy of which is dissipated in the primary switch snubber. Since the transformer is in-house built, the leakage inductance is quite high (2.4% of the primary inductance for the current prototype), the overall efficiency of the converter could be significantly improved by using an industrially made transformer.

VII. CONCLUSION

A key challenge of the ac-PV modules, in order to prove that this technology is a viable and cost-effective solution is the maximization of their efficiency without increased cost or reduced reliability. In this paper, the derivation of the analytical equations of the flyback inverter operated in improved BCM (i-BCM) for low THD was presented. Using those equations, the power dissipation of each converter component was calculated. A methodology to improve the performance of the converter by properly selecting all of the system parameters during the design phase, in order to maximize the weighted efficiency of the converter was described. Finally it was applied to a laboratory prototype, the experimental results of which validated the mathematical analysis.

APPENDIX A

In order to calculate the average and RMS values of the primary and secondary transformer currents, we have to calculate the following ratios:

$$S1_p\left(\frac{\lambda}{n}\right) = \frac{\sum_{i=0}^w \sin^p \theta_{i-1}}{\sum_{i=0}^w \left(\frac{\lambda}{n} + \sin \theta_{i-1}\right)} \quad (62)$$

$$S2_p\left(\frac{\lambda}{n}\right) = \frac{\sum_{i=0}^w \sin^p \theta_{i-1}}{\sum_{i=0}^w \left(\frac{\lambda}{n} + \sin \theta_{i-1}\right)^2}. \quad (63)$$

A. Calculation of $S1_p\left(\frac{\lambda}{n}\right)$

According to [19], [35] and using any mathematical software, it can be proven that:

$$S1_p\left(\frac{\lambda}{n}\right) = \frac{\sum_{i=0}^w \sin^p \theta_{i-1}}{\sum_{i=0}^w \left(\frac{\lambda}{n} + \sin \theta_{i-1}\right)} \approx \frac{1}{\pi} \cdot \int_0^\pi \frac{\sin^p \theta}{\left(\frac{\lambda}{n} + \sin \theta\right)} \cdot d\theta \quad (64)$$

$$= \frac{1}{\pi} \cdot \int_0^\pi \sin^{(p-1)} \theta \cdot d\theta - \left(\frac{\lambda}{n}\right) \cdot \left[\frac{1}{\pi} \cdot \int_0^\pi \frac{\sin^{(p-1)} \theta}{\left(\frac{\lambda}{n} + \sin \theta\right)} \cdot d\theta \right]$$

and so a recursive formula is derived:

$$S1_p\left(\frac{\lambda}{n}\right) = S_{(p-1)} - \left(\frac{\lambda}{n}\right) \cdot S1_{(p-1)}\left(\frac{\lambda}{n}\right). \quad (65)$$

According to [52] page 412 equations (3.621.3) and (3.621.4):

$$S_{(p-1)} = \frac{1}{\pi} \int_0^\pi \sin^{(p-1)} \theta \cdot d\theta$$

$$= \begin{cases} 1 & \text{for } (p-1)=0 \\ \frac{2}{\pi} & \text{for } (p-1)=1 \\ \frac{(2q-1)!!}{(2q)!!} = \frac{1 \cdot 3 \cdot 5 \cdot 7 \cdots (2q-1)}{2 \cdot 4 \cdot 6 \cdot 8 \cdots (2q)} & \text{for } (p-1)=2q \text{ and } q \geq 1 \\ \frac{(2q)!!}{(2q+1)!!} \cdot \frac{2}{\pi} = \frac{2 \cdot 4 \cdot 6 \cdot 8 \cdots (2q)}{1 \cdot 3 \cdot 5 \cdot 7 \cdots (2q+1)} \cdot \frac{2}{\pi} & \text{for } (p-1)=2q+1 \text{ and } q \geq 1 \end{cases} \quad (66)$$

whereas $S1_0\left(\frac{\lambda}{n}\right)$ is given by [19], [35] and is:

$$S1_0\left(\frac{\lambda}{n}\right) = \frac{1}{\pi} \cdot \int_0^\pi \frac{1}{\left(\frac{\lambda}{n} + \sin \theta\right)} d\theta$$

$$= \begin{cases} \frac{2}{\pi \sqrt{\left(\frac{\lambda}{n}\right)^2 - 1}} \cdot \arctan \sqrt{\left(\frac{\lambda}{n}\right)^2 - 1}, & \text{for } \frac{\lambda}{n} > 1 \\ \frac{2}{\pi}, & \text{for } \frac{\lambda}{n} = 1 \\ \frac{2}{\pi \sqrt{1 - \left(\frac{\lambda}{n}\right)^2}} \cdot \operatorname{arctanh} \sqrt{1 - \left(\frac{\lambda}{n}\right)^2}, & \text{for } 0 < \frac{\lambda}{n} < 1. \end{cases} \quad (67)$$

Fig. 16 shows $S1_p$ as a function of λ/n .

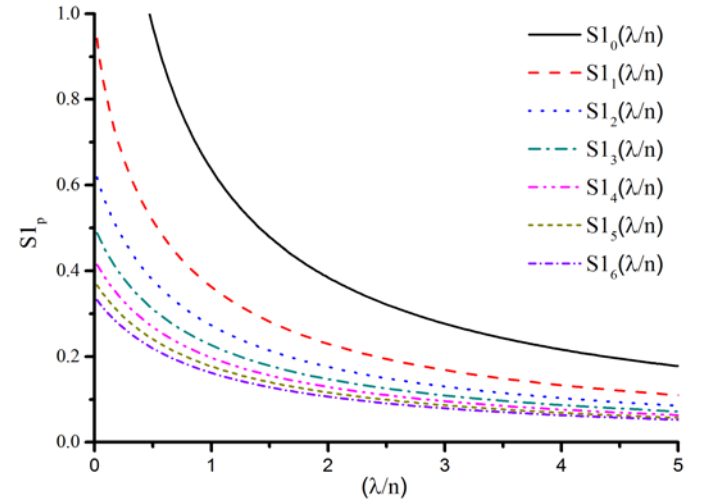


Fig. 16. $S1_p$ as a function of λ/n .

B. Calculation of $S2_p\left(\frac{\lambda}{n}\right)$

According to [19], [35] and using any mathematical software, it can be proven that:

$$\begin{aligned}
 S2_p\left(\frac{\lambda}{n}\right) &= \frac{\sum_{i=0}^w \sin^p \theta_{i-1}}{\sum_{i=0}^w \left(\frac{\lambda}{n} + \sin \theta_{i-1}\right)^2} \approx \frac{1}{\pi} \cdot \int_0^\pi \frac{\sin^p \theta}{\left(\frac{\lambda}{n} + \sin \theta\right)^2} \cdot d\theta \\
 &= \frac{1}{\pi} \cdot \int_0^\pi \frac{\sin^{(p-1)} \theta}{\left(\frac{\lambda}{n} + \sin \theta\right)} \cdot d\theta - \left(\frac{\lambda}{n}\right) \cdot \left[\frac{1}{\pi} \cdot \int_0^\pi \frac{\sin^{(p-1)} \theta}{\left(\frac{\lambda}{n} + \sin \theta\right)^2} \cdot d\theta \right] \\
 &= -\frac{1}{2} \cdot \left[\left(1\right) \frac{\tan^{(2 \cdot 0 + 1)}\left(\frac{\pi - \theta}{4} - \frac{\theta}{2}\right)}{2 \cdot 0 + 1} + \left(1\right) \frac{\tan^{(2 \cdot 1 + 1)}\left(\frac{\pi - \theta}{4} - \frac{\theta}{2}\right)}{2 \cdot 1 + 1} \right]^\pi \\
 &= -\frac{1}{2 \cdot \pi} \cdot \left\{ \left[\tan\left(-\frac{\pi}{4}\right) + \frac{1}{3} \cdot \tan^3\left(-\frac{\pi}{4}\right) \right] - \left[\tan\left(\frac{\pi}{4}\right) + \frac{1}{3} \cdot \tan^3\left(\frac{\pi}{4}\right) \right] \right\} = \frac{4}{3 \cdot \pi}.
 \end{aligned} \tag{68} \tag{72}$$

and so a recursive formula is derived:

$$S2_p\left(\frac{\lambda}{n}\right) = S1_{(p-1)}\left(\frac{\lambda}{n}\right) \cdot S2_{(p-1)}\left(\frac{\lambda}{n}\right). \tag{69}$$

$S1_{(p-1)}\left(\frac{\lambda}{n}\right)$ is calculated as shown above, whereas

$$S2_0\left(\frac{\lambda}{n}\right) = \frac{1}{\pi} \cdot \int_0^\pi \frac{1}{\left(\frac{\lambda}{n} + \sin \theta\right)^2} \cdot d\theta \tag{70}$$

is calculated based on [52] page 170 equation (2.551.1) and page 180 equation (2.555.1).

In particular, for $k = \frac{\lambda}{n} \neq 1$ and $n=2$, according to [52] equation (2.555.1)

$$\begin{aligned}
 S2_0(k) &= \frac{1}{(2 \cdot 1) \cdot (k^2 - 1^2)} \left[\frac{(1 \cdot 1 - k \cdot 0) \cdot \cos \theta}{(k+1 \cdot \sin \theta)^{(2-1)}} + \int_0^\pi \frac{(1 \cdot k - 0 \cdot 1) \cdot (2-1) + (k \cdot 0 - 1 \cdot 1) \cdot (2-2) \cdot \cos \theta}{(k+1 \cdot \sin \theta)^{(2-1)}} \cdot d\theta \right] \\
 &= \frac{1}{(k^2 - 1)} \left\{ \left[\frac{\cos \theta}{(k + \sin \theta)} \right]_0^\pi + \int_0^\pi \frac{k}{(k + \sin \theta)} \cdot d\theta \right\} \\
 &= \frac{1}{(k^2 - 1)} \left[-\frac{2}{k\pi} + k \cdot S1_0(k) \right]
 \end{aligned} \tag{71}$$

Moreover, for $k = \frac{\lambda}{n} = 1$ and $n=2$, according to [52] equation (2.555.5)

$$\begin{aligned}
 S2_0(k) &= -\frac{1}{2^{(2-1)}} \cdot \left[2 \cdot 0 \cdot \sum_{m=0}^{2-2} \binom{2-2}{m} \frac{\tan^{(2-m+1)}\left(\frac{\pi - \theta}{4} - \frac{\theta}{2}\right)}{2 \cdot m + 1} + (1-0) \right. \\
 &\quad \left. \cdot \sum_{m=0}^{2-1} \binom{2-1}{m} \frac{\tan^{(2-m+1)}\left(\frac{\pi - \theta}{4} - \frac{\theta}{2}\right)}{2 \cdot m + 1} \right]^\pi
 \end{aligned}$$

Fig. 17 shows $S2_p$ as a function of λ/n .

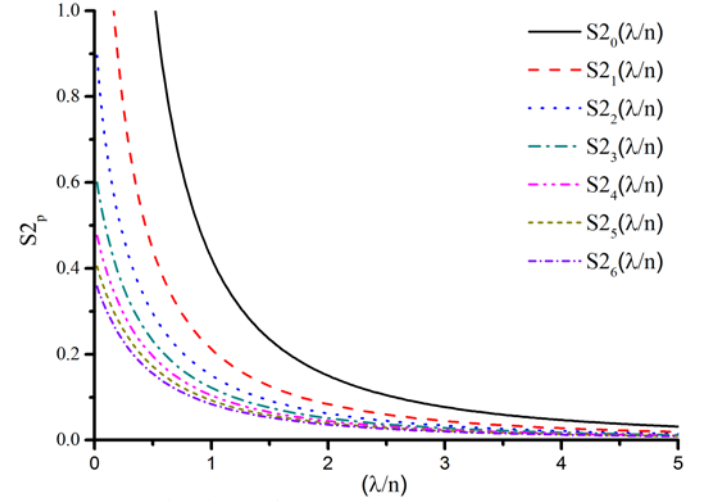


Fig. 17. $S2_p$ as a function of λ/n .

C. Calculation of $\Sigma I_{pri,avg}$

According to the previous analysis, we have:

$$\begin{aligned}
 \Sigma I_{pri,avg} &= \left(\frac{\lambda}{n}\right)^2 \cdot S2_2\left(\frac{\lambda}{n}\right) + 2 \cdot \left(\frac{\lambda}{n}\right) \cdot S2_3\left(\frac{\lambda}{n}\right) + S2_4\left(\frac{\lambda}{n}\right) \\
 &= \left(\frac{\lambda}{n}\right)^2 \cdot S2_2\left(\frac{\lambda}{n}\right) + 2 \cdot \left(\frac{\lambda}{n}\right) \cdot S2_3\left(\frac{\lambda}{n}\right) + S2_4\left(\frac{\lambda}{n}\right) \\
 &= \left(\frac{\lambda}{n}\right)^2 \cdot S2_2\left(\frac{\lambda}{n}\right) + 2 \cdot \left(\frac{\lambda}{n}\right) \cdot S2_3\left(\frac{\lambda}{n}\right) + S1_3\left(\frac{\lambda}{n}\right) - \left(\frac{\lambda}{n}\right) \\
 &\quad \cdot S2_3\left(\frac{\lambda}{n}\right) \\
 &= \left(\frac{\lambda}{n}\right)^2 \cdot S2_2\left(\frac{\lambda}{n}\right) + \left(\frac{\lambda}{n}\right) \cdot S2_3\left(\frac{\lambda}{n}\right) + S1_3\left(\frac{\lambda}{n}\right) = \\
 &= \left(\frac{\lambda}{n}\right)^2 \cdot S2_2\left(\frac{\lambda}{n}\right) + \left(\frac{\lambda}{n}\right) \cdot \left[S1_2\left(\frac{\lambda}{n}\right) - \left(\frac{\lambda}{n}\right) \cdot S2_2\left(\frac{\lambda}{n}\right) \right] \\
 &\quad + S1_3\left(\frac{\lambda}{n}\right) \\
 &= \left(\frac{\lambda}{n}\right)^2 \cdot S2_2\left(\frac{\lambda}{n}\right) + \left(\frac{\lambda}{n}\right) \cdot S1_2\left(\frac{\lambda}{n}\right) - \left(\frac{\lambda}{n}\right)^2 \cdot S2_2\left(\frac{\lambda}{n}\right) \\
 &\quad + S1_3\left(\frac{\lambda}{n}\right) \\
 &= \left(\frac{\lambda}{n}\right) \cdot S1_2\left(\frac{\lambda}{n}\right) + S1_3\left(\frac{\lambda}{n}\right) = \left(\frac{\lambda}{n}\right) \cdot S1_2\left(\frac{\lambda}{n}\right) \\
 &\quad + S2_2\left(\frac{\lambda}{n}\right) - \left(\frac{\lambda}{n}\right) \cdot S1_2\left(\frac{\lambda}{n}\right)
 \end{aligned}$$

$$\Sigma I_{pri,avg} = S_2 \left(\frac{\lambda}{n} \right) = \frac{1}{2}. \quad (73)$$

D. Calculation of $\Sigma I_{pri,rms}$

$$\begin{aligned} \Sigma I_{pri,rms} &= \left(\frac{\lambda}{n} \right) \cdot S_3 \left(\frac{\lambda}{n} \right) + S_4 \left(\frac{\lambda}{n} \right) \\ &= \left(\frac{\lambda}{n} \right) \cdot \frac{2}{\pi} \cdot \frac{2}{3} + \frac{1 \cdot 3}{2 \cdot 4} = \frac{4}{3 \cdot \pi} \cdot \left(\frac{\lambda}{n} \right) + \frac{3}{8}. \end{aligned} \quad (74)$$

After some mathematical calculations, based on the sequence that was demonstrated for the determination of $\Sigma I_{pri,avg}$, using the recursive formulas:

$$\Sigma I_{pri,rms} = \frac{4}{3 \cdot \pi} \cdot \left(\frac{\lambda}{n} \right) + \frac{3}{8}. \quad (75)$$

E. Calculation of $\Sigma I_{sec,avg}$

$$\begin{aligned} \Sigma I_{sec,avg} &= \left(\frac{\lambda}{n} \right)^2 \cdot S_2 \left(\frac{\lambda}{n} \right) + 2 \cdot \left(\frac{\lambda}{n} \right) \cdot S_2 \left(\frac{\lambda}{n} \right) + S_2 \left(\frac{\lambda}{n} \right) \\ &= \left(\frac{\lambda}{n} \right)^2 \cdot S_2 \left(\frac{\lambda}{n} \right) + 2 \cdot \left(\frac{\lambda}{n} \right) \cdot S_2 \left(\frac{\lambda}{n} \right) + S_2 \left(\frac{\lambda}{n} \right). \end{aligned} \quad (76)$$

After some mathematical calculations, based on the sequence that was demonstrated for the determination of $\Sigma I_{pri,avg}$, using the recursive formulas:

$$\Sigma I_{sec,avg} = S_1 \left(\frac{\lambda}{n} \right) = \frac{2}{\pi}. \quad (77)$$

F. Calculation of $\Sigma I_{sec,rms}$

$$\begin{aligned} \Sigma I_{sec,rms} &= \left(\frac{\lambda}{n} \right)^3 \cdot S_2 \left(\frac{\lambda}{n} \right) + 3 \cdot \left(\frac{\lambda}{n} \right)^2 \cdot S_2 \left(\frac{\lambda}{n} \right) + 3 \cdot \left(\frac{\lambda}{n} \right) \\ &\cdot S_2 \left(\frac{\lambda}{n} \right) + S_2 \left(\frac{\lambda}{n} \right) = \left(\frac{\lambda}{n} \right)^3 \cdot S_2 \left(\frac{\lambda}{n} \right) + 3 \cdot \left(\frac{\lambda}{n} \right)^2 \\ &\cdot S_2 \left(\frac{\lambda}{n} \right) + 3 \cdot \left(\frac{\lambda}{n} \right) \cdot S_2 \left(\frac{\lambda}{n} \right) + S_2 \left(\frac{\lambda}{n} \right). \end{aligned} \quad (78)$$

After some mathematical calculations, based on the sequence that was demonstrated for the determination of $\Sigma I_{pri,avg}$, using the recursive formulas:

$$\begin{aligned} \Sigma I_{sec,rms} &= \left(\frac{\lambda}{n} \right) \cdot S_2 \left(\frac{\lambda}{n} \right) + S_3 \left(\frac{\lambda}{n} \right) = \left(\frac{\lambda}{n} \right) \cdot \frac{1}{2} + \frac{2}{\pi} \cdot \frac{2}{1 \cdot 3} \\ &= \frac{1}{2} \cdot \left(\frac{\lambda}{n} \right) + \frac{4}{3 \cdot \pi} = \frac{1}{2} \cdot \left(\frac{\lambda}{n} \right) + \frac{4}{3 \cdot \pi}. \end{aligned} \quad (79)$$

APPENDIX B

For the calculation of $\Sigma P_{SL,pri}$:

$$\begin{aligned} \Sigma P_{SL,sw,pri} &= \left(\frac{\lambda}{n} \right)^2 \cdot S_2 \left(\frac{\lambda}{n} \right) + 2 \cdot \left(\frac{\lambda}{n} \right) \cdot S_2 \left(\frac{\lambda}{n} \right) + S_2 \left(\frac{\lambda}{n} \right) \\ &= \left(\frac{\lambda}{n} \right)^2 \cdot S_2 \left(\frac{\lambda}{n} \right) + 2 \cdot \left(\frac{\lambda}{n} \right) \cdot S_2 \left(\frac{\lambda}{n} \right) + S_2 \left(\frac{\lambda}{n} \right). \end{aligned} \quad (80)$$

After some mathematical calculations, based on the sequence that was demonstrated for the determination of $\Sigma I_{pri,avg}$, using the recursive formulas:

$$\Sigma P_{SL,sw,pri} = S_1 \left(\frac{\lambda}{n} \right) = \frac{n \cdot 2}{\lambda \cdot \pi}. \quad (81)$$

APPENDIX C

A. Calculation of $\Sigma T_{s,avg}$

$$\begin{aligned} \Sigma T_{s,avg} &= \left(\frac{\lambda}{n} \right)^4 \cdot S_2 \left(\frac{\lambda}{n} \right) + 4 \cdot \left(\frac{\lambda}{n} \right)^3 \cdot S_2 \left(\frac{\lambda}{n} \right) + 6 \cdot \left(\frac{\lambda}{n} \right)^2 \\ &\cdot S_2 \left(\frac{\lambda}{n} \right) + 4 \cdot \frac{\lambda}{n} \cdot S_2 \left(\frac{\lambda}{n} \right) + S_2 \left(\frac{\lambda}{n} \right). \end{aligned} \quad (82)$$

After some mathematical calculations, based on the sequence that was demonstrated for the determination of $\Sigma I_{pri,avg}$, using the recursive formulas:

$$\Sigma T_{s,avg} = \left(\frac{\lambda}{n} \right)^2 \cdot S_0 \left(\frac{\lambda}{n} \right) + 2 \cdot \frac{\lambda}{n} \cdot S_1 \left(\frac{\lambda}{n} \right) + S_2 \left(\frac{\lambda}{n} \right) = \left(\frac{\lambda}{n} \right)^2 + \frac{4}{\pi} \cdot \frac{\lambda}{n} + \frac{1}{2}. \quad (83)$$

B. Calculation of minimum and maximum switching frequencies

Using (13), the minimum switching frequency occurs at $\omega t = 90^\circ$ and the maximum switching frequency at $\omega t = 0^\circ$. So:

$$f_{s,max} = \frac{1}{T_{s,min}} = \frac{1}{T_{s,i} \Big|_{\omega t = 0}} = \frac{1}{\frac{t_{on,p}}{1 + \frac{\lambda}{n}} \left(\sin 0^\circ + \frac{\lambda}{n} \right)^2} = \frac{1}{t_{on,p}} \frac{1 + \frac{\lambda}{n}}{\left(\frac{\lambda}{n} \right)^2} \quad (84)$$

$$f_{s,min} = \frac{1}{T_{s,max}} = \frac{1}{T_{s,i} \Big|_{\omega t = 90^\circ}} = \frac{1}{\frac{t_{on,p}}{1 + \frac{\lambda}{n}} \left(\sin 90^\circ + \frac{\lambda}{n} \right)^2} = \frac{1}{t_{on,p}} \frac{1}{\left(1 + \frac{\lambda}{n} \right)}. \quad (85)$$

So, based on (49) and (84), (85) the ratios (51) and (52) are calculated respectively and are illustrated in Figs. 18 and 19 for different values of λ and n . We can observe that for a given value of λ , the increase on the transformer turns ratio n , leads to a drastic increase of the maximum switching frequency, whereas the minimum switching frequency is slightly decreased.

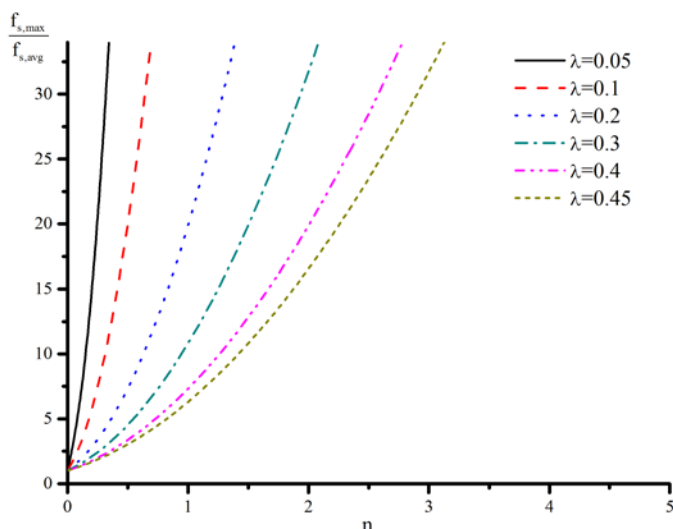


Fig. 18. Maximum/average switching frequency ratio as a function of n for different values of λ .

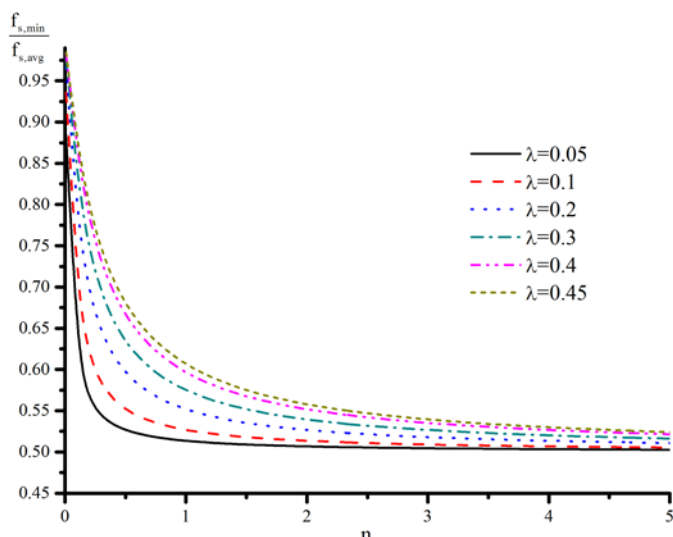


Fig. 19. Minimum/average switching frequency ratio as a function of n for different values of λ .

REFERENCES

- [1] R. H. Wills, F. E. Hall, S. J. Strong and J. H. Wohlgemuth, "The ac photovoltaic module," *Conf. Rec. 25th IEEE Photovoltaic Spec. Conf.*, Washington, DC, 13-17 May 1996, pp. 1231-1234.
- [2] S. B. Kjaer, J. K. Pedersen and F. Blaabjerg, "A review of single-phase grid-connected inverters for photovoltaic modules," *IEEE Trans. Ind. Appl.*, vol. 41, no. 5, pp. 1292-1306, Sep./Oct. 2005.
- [3] L. Quan and P. Wolfs, "A review of the single phase photovoltaic module integrated converter topologies with three dc link configurations," *IEEE Trans. on Power Electron.*, vol. 23, no. 3, pp. 1320-1333, May 2008.
- [4] D. Meneses, F. Blaabjerg, O. Garcia and J. Cobos, "Review and comparison of step-up transformerless topologies for photovoltaic ac-module application," *IEEE Trans. Power Electron.*, vol. 28, no. 6, pp. 2649-2662, Jun. 2013.
- [5] T. Freddy, N. A. Rahim, W. P. Hew and H. S. Che, "Comparison and Analysis of Single-Phase Transformerless Grid-Connected PV Inverters," *IEEE Trans. on Power Electron.*, vol. 29, no. 10, pp. 5358-5369, Oct 2014.
- [6] P. Sharma and V. Agarwal, "Exact maximum power point tracking of grid connected partially shaded pv source using current compensation concept," *IEEE Trans. Power Electron.*, accepted for publication.
- [7] N. Kasa, T. Iida, and L. Chen, "Flyback inverter controlled by sensorless current MPPT for photovoltaic power system," *IEEE Trans. Ind. Electron.*, vol. 52, no. 4, pp. 1145-1152, Aug. 2005.
- [8] S. Ozturk and I. Cadirci, "DSPIC microcontroller based implementation of a flyback PV microinverter using Direct Digital Synthesis," *IEEE Energy Conv. Congr. and Exposition (ECCE)*, 15-19 Sept. 2013, pp. 3426-3433.
- [9] A. Moallem, D. Yazdani, A. Bakhshai and P. Jain, "An anti-islanding protection scheme for grid-connected distributed power generation systems," *Int. Conf. Power, Control and Embedded Systems (ICPCES)*, 29 Nov.-1 Dec 2010.
- [10] T. Mizuno, Y. Noda, H. Koizumi, K. Nagasaka, K. Kurokawa and H. Kobayashi, "The experimental results of an islanding detection method for Japanese AC modules," *Proc. 3rd World Conf. Photovoltaic Energy Conv.*, vol.2, 18 May 2003, pp. 2058-2061.
- [11] A.C. Kyritsis, N. P. Papanikolaou and E. C. Tatakis, "A novel Parallel Active Filter for Current Pulsation Smoothing on single stage grid-connected AC-PV modules," *European Conf. Power Electr. and Appl.*, 2-5 Sept. 2007, pp.1-10.
- [12] H. Hu, S. Harb, N. Kutkut, I. Batarseh and Z. J. Shen, "A review of power decoupling techniques for microinverters with three different decoupling capacitor locations in PV systems," *IEEE Trans. Power Electron.*, vol. 28, no. 6, pp. 2711-2726, Jun. 2013.
- [13] H. Hu, S. Harb, N. H. Kutkut, Z. J. Shen and I. Batarseh, "A single-stage microinverter without using electrolytic capacitors," *IEEE Trans. Power Electron.*, vol. 28, no. 6, pp. 2677-2687, Jun. 2013.
- [14] H. Hu, S. Harb, X. Fang, D. Zhang, Q. Zhang, Z. J. Shen and I. Batarseh, "A three-port flyback for PV microinverter applications with power pulsation decoupling capability," *IEEE Trans. Power Electron.*, vol. 27, no. 9, pp. 3953-3964, Sep. 2012.
- [15] T. Shimizu, K. Wada and N. Nakamura, "Flyback-type single-phase utility interactive inverter with power pulsation decoupling on the DC input for an AC photovoltaic module system," *IEEE Trans. Power Electron.*, vol. 21, no. 5, pp. 1264-1272, Sep. 2006.
- [16] F. Deveci, S. Zengin and M. Boztepe, "Volt-second-based control method for discontinuous conduction mode flyback micro-inverters to improve total harmonic distortion," *IET Power Electron.*, vol. 6, no. 8, pp. 1600-1607, Sep. 2013.
- [17] S. Zengin, F. Deveci and M. Boztepe, "Decoupling capacitor selection in DCM flyback PV microinverters considering harmonic distortion," *IEEE Trans. Power Electron.*, vol. 28, no. 2, pp. 816-825, Feb. 2013.
- [18] Y.-H. Ji, D.-Y. Jung, J.-G. Kim, Y.-H. Kim and C.-Y. Won, "A phase lagging compensation for output current of DCM flyback based PV micro-inverters," *7th Int. Power Electron. and Motion Control Conf. (IPEMC)*, 2-5 June 2012, vol. 2, pp. 1247-1251.
- [19] A. Ch. Kyritsis, E. C. Tatakis and N. P. Papanikolaou, "Optimum design of the current-source flyback inverter for decentralized grid-connected photovoltaic systems," *IEEE Trans. Energy Conv.*, vol.23, no.1, pp. 281-293, Mar. 2008.
- [20] N. Kasa, T. Iida and C. Liang, "Flyback inverter controlled by sensorless current mppt for photovoltaic power system," *IEEE Trans. Ind. Electron.*, vol. 52, no. 4, pp.1145-1152, Aug. 2005.
- [21] Y.-H. Ji, D.-Y. Jung, J.-H. Kim, T.-W. Lee and C.-Y. Won, "A current shaping method for PV-AC module DCM-flyback inverter under CCM operation," *Proc. 8th Int. Conf. Power Electron.-ECCE Asia*, 30 May-3 Jun. 2011, pp. 2598-2605 2011.
- [22] Y. Li and R. Oruganti, "A low cost flyback CCM inverter for ac module application," *IEEE Trans. Power Electron.*, vol. 27, no. 3, pp. 1295-1303, Mar. 2012.
- [23] F. F. Edwin, W. Xiao and V. Khadkikar, "Dynamic modeling and control of interleaved flyback module-integrated converter for PV power applications," *IEEE Trans. Ind. Electron.*, vol. 61, no. 3, pp. 1377-1388, Mar. 2014.
- [24] M. Gao, M. Chen, C. Zhang and Z. Qian, "Analysis and implementation of an improved flyback inverter for photovoltaic ac module applications," *IEEE Trans. Power Electron.*, vol. 29, no. 7, pp. 3428-3444, Jul. 2014.
- [25] A. C. Nanakos, "Optimal design of the flyback current source inverter for ac/pv modules applications," PhD Thesis, University of Patras, Greece, Oct. 2012 (available in greek).
- [26] N. Sukesh, M. Pahlevaninezhad and P. K. Jain, "Analysis and implementation of a single-stage flyback PV microinverter with soft switching," *IEEE Trans. Ind. Electron.*, vol. 61, no. 4, pp. 1819-1833, Apr. 2014.

- [27] N. Kasa, T. Iida and A. K. S. Bhat, "Zero-voltage transition flyback inverter for small scale photovoltaic power system," *Proc. IEEE Power Electron. Spec. Conf. (PESC)*, 16 Jun. 2005, pp. 2098-2103.
- [28] J.-S. Kang, Y.-H. Kim, S.-J. Youn, C.-Y. Won and Y.-C. Jung, "Active clamp flyback inverter considering leakage inductance of transformer for photovoltaic AC modules," *IEEE Vehicle Power and Propulsion Conf. (VPPC)*, 9-12 Oct. 2012, pp. 1379-1383.
- [29] Y.-H. Kim, Y.-H. Ji, J.-G. Kim, Y.-C. Jung, and C.-Y. Won, "A new control strategy for improving weighted efficiency in photovoltaic ac module-type interleaved flyback inverters," *IEEE Trans. Power Electron.*, vol. 28, no. 6, pp. 2688-2699, Jun. 2013.
- [30] Y.-C. Hsieh, M.-R. Chen and H.-L. Cheng, "An interleaved flyback converter featured with zero-voltage transition," *IEEE Trans. Power Electron.*, vol. 26, no. 1, pp. 79-84, Jan. 2011.
- [31] Z. Zhang, X.-F. He and Y.-F. Liu, "An optimal control method for photovoltaic grid-tied-interleaved flyback microinverters to achieve high efficiency in wide load range," *IEEE Trans. Power Electron.*, vol. 28, no. 11, pp. 5074-5087, Nov. 2013.
- [32] Zhang, M. Chen, W. Chen, C. Jiang and Z. Qian, "Analysis and Implementation of Phase Synchronization Control Strategies for BCM Interleaved Flyback Micro-inverters," *IEEE Trans. Power Electron.*, accepted for publication.
- [33] T. V. Thang, N. M. Thao, J.-H. Jang and J.-H. Park, "Analysis and design of grid-connected photovoltaic systems with multiple-integrated converters and a pseudo-dc-link inverter," *IEEE Trans. Ind. Electron.*, vol. 61, no. 7, pp. 3377-3386, Jul. 2014.
- [34] *Photovoltaic systems - Power conditioners - Procedure for measuring efficiency*, European Standard EN 61683, 2000.
- [35] A. C. Nanakos, E. C. Tatakis and N. P. Papanikolaou, "A weighted-efficiency-oriented design methodology of flyback inverter for ac photovoltaic modules," *IEEE Trans. Power Electron.*, vol. 27, no. 7, pp. 3221- 3233, Jul. 2012.
- [36] J.-H. Jang, S.-K. Sul and Y.-C. Son, "Current measurement issues in sensorless control algorithm using high frequency signal injection method," *Conf. Rec. 8th IAS Annu. Meet. Ind. Appl. Conf.*, 12-16 Oct. 2003, vol.2, pp.1134-1141.
- [37] R.W.Erickson and D.Maksimovic, *Fundamentals of Power Electronics*. Norwell, MA: Kluwer, 2001
- [38] Duncan A. Grant and John Gowar, "Power Mosfets, Theory and Applications," Wiley-Interscience, 1989, ch. 4.
- [39] S. Hui and J. Zhu., "Magnetic hysteresis modeling and simulation using the Preisach theory and TLM technique," *Proc. IEEE 25th Annu. Power Electron. Spec. Conf.*, Taipei, Taiwan, vol. 2, Jun. 20-25 1994, pp. 837-842.
- [40] D. C. Jiles and D. L. Atherton, "Theory of ferromagnetic hysteresis (invited)," *Journ. Appl. Phys.*, vol.55, no.6, pp.2115-2120, Mar. 1984.
- [41] Roshen W.A., "A Practical, Accurate and Very General Core Loss Model for Nonsinusoidal Waveforms," *IEEE Trans. Power Electron.*, vol.22, no.1, pp.30-40, Jan. 2007.
- [42] J. Reinert, A. Brockmeyer and R. W. A. A. De Doncker, "Calculation of losses in ferro- and ferrimagnetic materials based on the modified Steinmetz equation," *IEEE Trans. Ind. Appl.*, vol.37, no.4, pp.1055-1061, Jul./Aug. 2001.
- [43] J. Li, T. Abdallah and C. R. Sullivan, "Improved calculation of core loss with nonsinusoidal waveforms," *Conf. Rec. 36th IEEE Ind. Appl. Conf.*, vol. 4, 30 Sep.-4 Oct. 2001, pp. 2203-2210.
- [44] K. Venkatachalam, C. R. Sullivan, T. Abdallah and H. Tacca, "Accurate prediction of ferrite core loss with nonsinusoidal waveforms using only Steinmetz parameters," *Proc. IEEE Comput. Power Electron. Conf.*, 2002, pp. 36-41.
- [45] S. Wolfram, *The mathematica book*, 5th ed. Champaign, IL: Wolfram Media, 2004.
- [46] J. M. Lopera, M. J. Prieto, J. Diaz and J. Garcia, "A Mathematical Expression to Determine Copper Losses in Switching-Mode Power Supplies Transformers Including Geometry and Frequency Effects," *IEEE Trans. on Power Electron.*, accepted for publication.
- [47] A. Roszkopf, E. Bar and C. Joffe, "Influence of Inner Skin- and Proximity Effects on Conduction in Litz Wires," *IEEE Trans. Power Electron.*, vol. 29, no. 10, pp. 5454 -5461, Oct. 2014.
- [48] G. S. Dimitrakakis, E. C. Tatakis and E. J. Rikos, "A semiempirical model to determine HF copper losses in magnetic components with nonlayered coils," *IEEE Trans. Power Electron.*, vol. 23, no. 6, pp. 2719-2728, Nov. 2008
- [49] N. P. Polyzos, E. C. Tatakis and A. N. Safacas, "A Novel method oriented to evaluate the real characteristics of practical buck zero-voltage switching quasi-resonant converters," *IEEE Trans. Power Electron.*, vol. 16, no 3, pp. 316-324, May 2001.
- [50] E. C. Tatakis and N. P. Polyzos, "A Novel method oriented to evaluate the real characteristics of practical boost zero-voltage switching quasi-resonant converters," *European Power Electron. and Drives Journal*, vol. 11, no 2, May 2001, pp. 25-33.
- [51] L. H. Dixon, *Magnetics Design for Switching Power Supplies*. Dallas, TX: Unitrode Seminars (TI), 2001.
- [52] S. Gradshteyn, I. M. Ryzhik and A. Jeffrey, "Table of Integrals, Series, and Products", 5th Edition, Academic Press Inc., Harcourt Brace & Company, Publishers, Copyright 1994.



Anastasios Ch. Nanakos was born in Thessaloniki, Greece, in 1981. He received the Dipl. and Ph.D. degrees from the University of Patras, Patras, Greece in 2005 and 2012 respectively, both in electrical and computer engineering.

He has worked as a Researcher and Teaching Assistant at the University of Patras and as a Laboratory Collaborator at the Technological Educational Institute of Patras. Currently, he is with Dyson Technology Ltd., in RDD. His current research interests include power electronic converters, electric motor drives, design optimization techniques, and other related topics.



Georgios C. Christidis (S'10) received the Dipl. degree in electrical and computer engineering from the University of Patras, Rion-Patras, Greece, in 2010 where he is currently working towards the PhD degree in voltage step-up converters.

His research interests include the analysis, design, simulation and construction of DC/DC and DC/AC converters for use in renewable energy systems, waste heat recovery systems and aeronautics and space applications.

Mr. Christidis is a member of the Technical Chamber of Greece.



Emmanuel C. Tatakis received the Dipl. degree in electrical engineering from the University of Patras, Rion-Patras, Greece, in 1981, and the Ph.D. degree in applied sciences from the University of Brussels, Brussels, Belgium, in 1989.

He is currently Professor with the Department of Electrical and Computer Engineering, University of Patras, Greece. His teaching activities include power electronics and electrical machines. His research interests include switch-mode power supplies, resonant converters, HF transformers, power factor correction, electric drive systems and electric vehicles, converters for renewable energy systems, voltage multipliers, educational methods in electrical machines and power electronics.

Dr.-Ing. E.C. Tatakis is also a member of the European Power Electronics Association (EPE) and the Technical Chamber of Greece.